MASARYK UNIVERSITY
FACULTY OF SCIENCE

Ph.D. Dissertation

BRNO 2023 SLAH ABDELLAOUI

MASARYK UNIVERSITY
FACULTY OF SCIENCE
DEPARTMENT OF THEORETICAL PHYSICS AND ASTROPHYSICS

Hydrodynamic modeling of stellar winds

Ph.D. Dissertation

Slah Abdellaoui

Supervisor: Prof. Mgr. Jiří Krtička, Ph.D. **Brno 2023**

Bibliographic Entry

Author: Slah Abdellaoui
Faculty of Science, Masaryk University
Department of Theoretical Physics and Astrophysics

Title of Thesis: Hydrodynamic modeling of stellar winds

Degree Programme: Physics

Field of Study: Theoretical Physics and Astrophysics

Supervisor: Prof. Mgr. Jiří Krtička, Ph.D.
Faculty of Science, Masaryk University
Department of Theoretical Physics and Astrophysics

Academic Year: 2023/2024

Number of Pages:

Keywords: stars: mass-loss – stars: evolution – stars: rotation – hydrodynamics – stars: polarization

Bibliografický záznam

Autor: Slah Abdellaoui
Přírodovědecká fakulta, Masarykova univerzita
Ústav teoretické fyziky a astrofyziky

Název práce: Hydrodynamika hvězdného větru horkých hvězd

Studijní program: Fyzika

Studijní obor: Teoretická fyzika a astrofyzika

Vedoucí práce: Prof. Mgr. Jiří Krtička, Ph.D.
Přírodovědecká fakulta, Masarykova univerzita
Ústav teoretické fyziky a astrofyziky

Akademický rok: 2023/2024

Počet stran:

Klíčová slova: hvězdy: ztráta hmoty – hvězdy: vývoj – hvězdy: rotace – hydrodynamika –hvězdy: polarizace

Abstract

The dynamics of winds around rotating hot stars, particularly the hottest and most massive stars of spectral types O, B, and WR, are of great interest to astronomers. These stars have powerful stellar winds that are believed to be driven by the scattering of the star's continuum radiation field. However, there are still many questions surrounding these winds, especially when it comes to their complex time variability and the influence of factors like rapid rotation, pulsation, and surface magnetic fields.

In order to gain a better understanding of these phenomena, this dissertation aims to model the dynamics of winds around rotating hot stars. By doing so, it seeks to synthesize theoretical observational diagnostics that can be compared to actual data. This approach will help to shed light on the behavior and characteristics of these winds, providing insights into the underlying physical processes at play in these massive, evolving stars.

The rotation of a star has several effects on its behavior. It introduces centrifugal force, which reduce the effective gravity of the star and cause it to become oblate, or flattened at the poles. This oblateness leads to changes in the radiative flux distribution, with the poles being heated more intensely than the equator. This phenomenon is known as gravity darkening. In addition to these effects, nonradial radiation forces are acting on matter around a rotating star. These forces point away from the equator and in the opposite direction of rotation, causing a net deflection of wind streamlines towards the poles. This is contrary to the "wind-compressed disk" model proposed by Bjorkman and Cassinelli, for Be stars, and Wolf Rayet stars. When the rotation rate of stars exceeds 80 % of the critical velocity, we have observed the formation of an equatorial disk in stars with low metallicity.

We have also used the analytical formula of Brown and McLean to calculate the linear polarization caused by electron scattering in Wolf-Rayet stars. We found that the two studied Wolf-Rayet stars meet the requirements to be progenitors of long gamma-ray bursts. Additionally, we examined the accuracy of the analytical formula by using Monte Carlo simulation to model the polarization in both optically thick and optically thin environments. The results were similar for low rotation rates, but there was a discrepancy at higher rotation rates. We also discovered that multiple scattering, modeled through Monte Carlo simulation, led to higher polarization at lower inclinations, specifically around 50 to 70 degrees. In the optically thin environment, both the analytical formula and the Monte Carlo simulation showed polarization proportional to the square of the sine of the inclination angle, as previously determined by Brown and McLean.

Abstrakt

Dynamika větrů rotujících horkých hvězd, zejména nejteplejších a nejhmotnějších hvězd spektrálních typů O, B a WR, je pro astronomii velmi zajímavá. Tyto hvězdy mají silné hvězdné větry, které jsou považovány za hnané rozptylem kontinuálního záření hvězdy. Nicméně stále existuje mnoho nezodpovězených otázek týkajících se těchto větru, zejména pokud jde o jejich složitou časovou proměnnost a vliv faktoru jako jsou rychlá rotace, pulzace a povrchová magnetická pole.

Abychom lépe porozuměli těmto jevum, klade si tato disertační práce za cíl namodelovat dynamiku větrů kolem rotujících horkých hvězd. Tímto zpusobem se snaží získat teoretické předpovědi pozorovatelných parametru, které mohou být porovnány se skutečnými daty. Tento přístup pomuže osvětlit chování a charakteristiky těchto větrů a poskytne nám informace o základních fyzikálních procesech, které se odehrávají v masivních vyvíjejících se hvězdách.

Rotace ovlivňuje chování hvězdy několika zpusoby. Vede ke vzniku odstředivé síly, která snižuje efektivní gravitaci hvězdy a zpusobuje její zploštění u pólu. Toto zploštění vede k změnám v rozložení zářivého toku, přičemž póly jsou intenzivněji zahřívány než rovník. Tento fenomén je znám jako gravitační ztemnění. Kromě těchto účinku pusobí na látku v okolí rotující hvězdy také neradiální složky zářivé síly. Tyto složky síly směřují od rovníku a ve směru opačném k rotaci, což zpusobuje celkové odchýlení proudnic větrů směrem k pólum. To je v rozporu s modelem "disku stlačeného větrem", který navrhli Bjorkman a Cassinelli pro hvězdy typů Be a Wolfova-Rayetova typů. Pokud rychlost rotace hvězd překročí 80 % kritické rychlosti, bylo zaznamenáno vytvoření rovníkového disku u hvězd s nízkou metalicitou.

Také jsme použili analytický vzorec Browna a McLeana pro výpočet lineární polarizace zpusobené rozptylem elektronu u hvězd Wolfova-Rayetova typů. Zjistili jsme, že obě zkoumané hvězdy Wolfova-Rayetova typů splňují požadavky na předchudce dlouhotrvajících gama-záblesku. Navíc jsme ověřovali přesnost analytického vzorce pomocí simulace Monte Carlo, která modelovala polarizaci v opticky tlustém i opticky tenkém prostředí. Výsledky obou metod byly podobné pro nízké rychlosti rotace, ale při vyšších rychlostech rotace se objevily odlišnosti. Zjistili jsme také, že vícenásobný rozptyl modelovaný prostřednictvím simulace Monte Carlo vede k vyšší polarizaci při nižších inklinacích, konkrétně kolem 50 až 70 stupňu. V opticky tenkém prostředí jak analytický vzorec, tak simulace Monte Carlo předpovídaly polarizaci, která byla úměrná kvadrátu sinu inklinace, jak předpověděli Brown a McLean.

© Slah Abdellaoui, Masaryk University, 2023

Acknowledgements

I would like to express my deepest gratitude and appreciation to all those who have contributed to the completion of this academic endeavor. Your support, guidance, and encouragement have been invaluable throughout this journey.

First and foremost, I would like to thank my supervisor, prof. Mgr. Jiří Krtička Ph.D and Mgr. Ing. arch. Petr Kurfürst Ph.D, for their unwavering support, expert knowledge, and guidance. Their dedication and commitment to my academic growth have been instrumental in shaping the direction and quality of this research. I am truly grateful for their mentorship and the valuable insights they have provided.

I would like to express my heartfelt gratitude to Prof. Stan Owocki and Dr. Asif ud-Doula for the incredible academic discussions we had. Your insights and expertise have greatly enriched my understanding of the subject matter. I would also like to extend my appreciation to Prof. Jon Sundvquist and Dr. Nicolas Moens for their unwavering support during my internship at KU Leuven University. Their guidance and encouragement have been invaluable throughout my journey. I am truly fortunate to have had such amazing mentors and supporters. Thank you all for your contributions to my academic and personal growth.

I would also like to extend my gratitude to the members of my thesis/dissertation committee, for their time, expertise, and constructive feedback. Their invaluable input and suggestions have helped me refine my research and enhance the overall quality of this work.

I am immensely grateful to the staff and faculty of science at Masaryk University, whose commitment to academic excellence and resources have greatly facilitated my research. The computing facilities team, technical support, and administrative personnel have been instrumental in providing the necessary resources and assistance throughout this project.

I would like to acknowledge the contributions of my colleagues and fellow researchers who have provided invaluable feedback, engaging discussions, and a supportive academic community. Their insights and diverse perspectives have greatly enriched my understanding and enhanced the overall quality of this work.

Furthermore, I am indebted to my family and friends for their unconditional love, support, and patience. Their unwavering belief in my abilities and their constant encouragement has been a source of inspiration and motivation.

Lastly, I would like to express my gratitude to all the participants and individuals who generously contributed their time, expertise, and insights to this research. Their willingness to participate and share their experiences has been crucial to the success of this study.

In conclusion, I am truly grateful to all those who have played a role in this academic endeavor. Your support, guidance, and encouragement have been invaluable, and I am thankful for the opportunity to have had such wonderful individuals by my side throughout this journey.

Thank you all for your contributions and for helping make this academic pursuit a reality.

Contents

Chapter 1. Introduction 1
1.1 Hot star winds 1
1.2 Effect of rotation 2
1.3 Instability of line-driven winds 3
1.4 Continuum polarization 3
1.5 Plan and goals of the thesis 4

Chapter 2. Theory of Stellar Winds 5
2.1 Gas dynamic 5
2.2 1D Spherically symmetric wind 5
2.3 The Sobolev approximation 8
2.3.1 Force due to electron scattering 9
2.3.2 Line force of single line 9
2.3.3 Force for an ensemble of lines 12
2.3.4 Solution in 1-D 13

Chapter 3. Rapid stellar rotation 15
3.1 Shape of rotating stars 15
3.2 Critical velocity 17
3.3 Theorem of von Zeipel 18
3.4 Espinosa Lara and Rieutord formulation 19

Chapter 4. Radiative transfer and polarization 23
4.1 Unpolarized radiation 23
4.2 Continuum polarization 24

Chapter 5. Numerical methods 29
5.1 Eulerian hydrodynamics 29
5.1.1 Simple advection 29
5.1.2 Riemann problem 31
5.1.3 Finite volume method 31
5.2 Godunov's method 32
5.2.1 WENO 33
5.2.2 Adaptive mesh refinement 34

5.3 Monte Carlo method of the radiative transfer 35
  5.3.1 Simple scattering 35
  5.3.2 Sampling technique 35
  5.3.3 Random number 36
  5.3.4 Computing flux and intensity 36
5.4 Scattering and polarization 37

Chapter 6. Modeling of stellar winds of rotating, hot and massive stars 41
6.1 Wind compressed disk 41
  6.1.1 Be stars 42
  6.1.2 Wolf Rayet stars 44
  6.1.3 Low metallicity stars 45
6.2 Effect of gravity darkening and nonradial forces 46
  6.2.1 Wolf Rayet stars 47
  6.2.2 Low metallicity stars 48
  6.2.3 VLT-FLAMES Tarantula Survey (VFTS) 52
6.3 Other codes 55

Chapter 7. Polarization due to electron scattering 57
7.1 Continuum polarization 57
7.2 Single scattering polarization 58
7.3 Effect of multiple-scattering 60
  7.3.1 Effect of rotation 61
  7.3.2 Effect of mass loss 62

Chapter 8. Conclusion and future work 65
8.1 Current work overview 65
8.2 Future work aspects 66

Bibliography 67

Chapter 1

Introduction

Massive stars are known to have stellar winds in their atmosphere; they play a dominant role in the mass and energy balance of the interstellar medium. In addition to mass loss, several other physical processes could also influence their evolution. The point of view of wind outflow has been studied extensively in past decades by many authors from rotation processes, pulsation, and magnetic field effects, for a better understanding of the importance of stellar winds in astrophysics.

In this context, we study the dynamic of stellar winds, the effect of rotation, and magnetic fields. By multidimensional hydrodynamic modeling of winds, we test and compare various theories of time-dependent and spherical wind outflow. In this chapter, we show the state-of-the-art and literature overview of stellar wind mechanisms, and we discuss model theory and observation of line-driven winds.

1.1 Hot star winds

To explain the radiative driven winds mechanism in Of stars, Castor, Abbott, and Klein (1975, hereinafter CAK) have introduced the line driven wind model, where the radiative force was expressed in terms of so-called CAK parameters. They expressed the line force as a function of local velocity gradient, and the model theory of Parker's solar wind (Parker, 1960) is no longer applicable for hot stars. Following this work, Friend and Abbott (1986, hereinafter FA) introduced the correction factor for the finite disk structure of the star as well as the centrifugal term due to stellar rotation. This modification improved the line-driven model theory to better fit with the observations, they observed an increase in the mass loss rate and a decrease in the ratio of terminal velocity to the escape speed in particular for B supergiants. In the same context Pauldrach, Puls, and Kudritzki (1986) checked the rotation effect on the mass loss using self-consistent model atmospheres of radiation-driven wind. In addition to rotational effect and finite disk correction factor, they employed the radiative transfer in the comoving frame (CMF) for the lines at different wavelengths, and they confirmed the validity of Sobolev approximation for the dynamic of stellar winds.

Massive stars of O- and early B-type exhibit effective temperatures that span a range from approximately 20,000 K to 50,000 K. This wide temperature range facilitates the occurrence of robust radiation-driven outflows known as line-driven winds (Crowther, 2007).

The precise rates at which these stars lose mass are of utmost importance for evolution models, as the majority of the mass loss during their relatively short lifetimes can be attributed to radiation pressure (Vink, de Koter, and Lamers, 2001). However, it is now universally acknowledged that the presence of density irregularities or "clumping" in O-star winds is nearly ubiquitous. This raises doubts regarding earlier estimates of mass loss that were derived from homogeneous models (Puls et al., 2006). Additionally, the existence of magnetic fields in a significant fraction of O-stars introduces further complexity, as the geometry of these fields can influence and modify the flow of the wind (Grunhut et al., 2017). These powerful wind outflows play a crucial role in the feedback mechanism of stars and contribute to the enrichment of the interstellar medium.

1.2 Effect of rotation

Stellar rotation does not produce only the centrifugal term in the frame of the star, but also could produce an equatorial outflowing disk for massive stars, in their work; Bjorkman and Cassinelli (1993) (BC) using FA model showed that the formation of an equatorial disk due to the rotation rate above the threshold depending on the ratio of the terminal velocity to the escape speed. They found that the rotation threshold changes depending on the stellar types, e.g for O stars the threshold can reach up to 90 % of the critical speed whereas for B2 stars the disk can form at 50 % to 60 % of the critical speed. The theoretical model explained the observation of the disk around massive rotating stars (Bjorkman and Cassinelli, 1993).

Using time-dependent 2.5-D hydrodynamic simulation, Owocki, Cranmer, and Blondin (1994) applied BC model to Be stars to simulate numerically the effect of rotation into the wind; as a result, the disk formation was confirmed with a slight difference in the opening angle. The numerical results showed other effects as well, which were not possible to incorporate analytically, including rotational distorted oblate stellar surface and the outward driving force.

Applying the wind compression model to different classes of massive stars, Ignace, Cassinelli, and Bjorkman (1996) found that the flow and density structure is mainly impacted by the ratio of stellar rotation to the critical speed and the threshold required for the disk formation. Two types of disk compression were discussed: i) wind-compressed disk (WCD) and ii) wind-compressed zone (WCZ) the latter can form even at lower rotation rates on the order of 10 %.

The radiative force using CAK formulation was considered in spherical symmetry radial dependent, adding the rotation which generates the centrifugal force, the latter acted as support for radiation to overcome the gravity. The flow becomes supersonic and with rotation rate threshold leads to a WCD. The model of Cranmer and Owocki (1995) reconsidered the model of the formulation of CAK line force in 3D where radiative force does not depend only on radius but has the angular components. Their work included also the effect of gravity darkening; the obtained results were in contradiction with the WCD model by BC. Instead of the flow being predicted by BC to be equatorward, it was observed to be poleward. Additionally, the density in the equatorial region was found to be reduced. This model has been confirmed by the numerical simulation by Owocki, Cranmer, and Gayley (1996) where the WCD is inhibited by non-radial forces.

1.3 Instability of line-driven winds

The line-driven wind instability (LDI) is an observed phenomenon in massive stars where their stellar winds become unstable as a result of the interaction between radiation and spectral lines in the stellar atmosphere. The instability was initially proposed by Lucy and Solomon (1970) and has since been extensively researched in the field of stellar astrophysics. The LDI occurs when the radiation pressure from the strong lines in the stellar spectrum interact with the stellar wind, leading to the emergence of density fluctuations and clumps in the wind. These density enhancements can have significant impacts on the dynamics of the stellar wind, including its acceleration and shaping, as well as the formation of structures like disks and shells around the star (Owocki and Puls, 1999). In order to ascertain the impact of LDI on the light variability exhibited by O stars, Krtička and Feldmeier (2018) employed the findings of hydrodynamic simulations to forecast the variations in light emitted by hot stars. The LDI plays a critical role in the processes of mass loss in massive stars and holds important implications for stellar evolution and the enrichment of the interstellar medium with stellar material. Here I would also say that LDI is a likely origin of shocks that lead to X-ray emission (Feldmeier et al., 1997) and that the clumps influence the observational properties of hot stars (Sundqvist, Puls, and Feldmeier, 2010; Šurlan et al., 2013).

1.4 Continuum polarization

Rotation does not only affect the change of the star's shape but it can modulate the light scattering of free electrons which will result the polarization of the radiation. Brown and McLean (1977) derived a general formula to calculate the polarization due to Thomson scattering, where the polarization depends mainly on the inclination and the shape of the star, the opacity of the medium, and the electron number density distribution. Following this work, Cassinelli, Nordsieck, and Murison (1987) introduced the depolarization factor for the finite size of stars; this factor has a slight effect on the value of the polarization as has been shown by Brown, Ignace, and Cassinelli (2000). Calculating the net polarization of Be and Wolf-Rayet stars, Fox (1993) found that the polarization is comparable to the observed values, however, showed some differences for Be stars. Comparing the single scattering model (Brown's model) with multiple scattering models using the Monte Carlo method, Townsend (2012) found that the two models are not consistent and concluded that single scattering can not be applied to clumpy stellar winds.

To interpret polarimetric data, McLean (1979), applied optically thin polarization formula on early emission-line stars, the observed polarization was comparable to the analytical formula. Line absorption results in a depolarization effect, where the attenuation factor has been included to explain the latter effect. In similar context, Friend and Cassinelli (1986) included the attenuation factor to compute the polarization of an optically thick axisymmetric winds in massive binaries.

Classical Wolf-Rayet (WR) stars are massive stars that have lost their hydrogen envelope during their evolution (Conti, 1975; Chiosi, Nasi, and Bertelli, 1979; Sander, Hamann, and Todt, 2012). These WR stars, which are fast rotating, may collapse into black holes and potentially generate long-duration gamma-ray bursts (Woosley, 1993).

Vink and de Koter (2005) proposed that these fast-rotating WR stars could be the progenitors of long-duration gamma-ray bursts. However, testing this model directly through observation is challenging due to the difficulties in accurately measuring the rotational velocities of Wolf-Rayet stars. One potential indirect method of testing the nature of gamma-ray burst progenitors is by estimating their rotational velocities through polarized light measurements.

Several methods exist for discerning interstellar polarization from intrinsic polarization in the observational context described by Schulte-Ladbeck (1994). Stevance et al. (2018) utilized Serkowski'slaw to analyze the interstellar polarization of WR93b and WR102. Their findings suggest that these two stars do not possess inherent polarization, thus no line effect could be observed. This lack of polarization could be due to the dilution of continuum polarization by unpolarized line flux. They established an upper limit on the rotational velocity, which is lower than the value determined by Sander et al. (2012) based on the shape of emission line profiles. These two stars, with their round emission line profiles, are potentially indicative of fast rotation. High rotational velocities are necessary for the formation of collapsars, which are presumed to be sources of long-duration gamma-ray bursts (Woosley, Eastman, and Schmidt, 1999).

1.5 Plan and goals of the thesis

In this work, we construct hydrodynamic models of hot-star winds and compare the results with previous studies. Furthermore, we analyze the linear polarization from single scattering and multiple scattering models. We start in Chapter 2 by presenting a review of the current state of radiatively driven stellar winds and focus on spherically symmetric solutions to the equations governing radiation hydrodynamics.

Rapid star rotation plays a critical role in the creation of nonspherical and temporally variable circumstellar structures. In Chapter 3 we discuss the impact of rapid stellar rotation on a spinning star's mass flow using the Roche model, along with the presence of von Zeipel gravity darkening. This results in a latitudinal variation where polar mass loss increases, while there is a projected gain near the equator due to decreasing centrifugal gravity. Additionally, rapid rotation can generate an axisymmetric stellar wind, potentially leading to nonzero polarization caused by electron scattering in the wind. The radiation transfer theory will be shown in Chapter 4, where we address the mathematical description for the radiative transfer equation and the Stokes vector of polarization.

In Chapter 5, we explore the numerical methods employed in astrophysics to solve the hydrodynamic equations and the equation of radiative transfer. Specifically, we focus on the finite volume method and the Monte Carlo method. The hydrodynamic simulation results will be presented in Chapter 6. Additionally, in Chapter 7, we delve into the topic of linear polarization from a point source, utilizing both single-scattering and multiple-scattering models. Chapter 8, at last, includes a concise summary and examination of the research presented in this dissertation. Moreover, it also provides an outline for future investigation that would tackle crucial inquiries regarding the radiation hydrodynamics of rotating hot-star winds.

Chapter 2

Theory of Stellar Winds

2.1 Gas dynamic

Stellar winds in massive stars are driven by radiative forces from the star's photosphere toward the interstellar medium. The motion of the gas outflow is described by solving the dynamical equations of mass, momentum, and energy conservation. These equations are given, mathematically, in terms of partial differential equations with a source term describing any external forces acting on the motion of the gas.

Neglecting the friction in the gas flow, the dynamics of the fluid are described by Euler equations (Cranmer, 1996; Castor, 2007), as follows:

$$\frac{\partial \rho}{\partial t} + \nabla(\rho \boldsymbol{v}) = 0, \tag{2.1}$$

$$\frac{\partial(\rho \boldsymbol{v})}{\partial t} + \nabla(\rho \boldsymbol{v}\boldsymbol{v}^T + P) = 0, \tag{2.2}$$

$$\frac{\partial(\rho e)}{\partial t} + \nabla[(\rho e + P)\boldsymbol{v}] = 0, \tag{2.3}$$

where ρ is the fluid density, $\boldsymbol{v}$ is the velocity vector, P is the pressure of the fluid, and $e = U_T + \boldsymbol{v}^2/2$ is the total energy per unit mass, and U_T is the thermal energy. As we can see, the equations are a set of conservation laws. In the above form, they are not complete. We need further relation for the pressure, to do so, we call the ideal gas law, in which the pressure is given by

$$P = (\gamma - 1)\rho U, \tag{2.4}$$

where γ is the specific heat constant. In the above equations, we can include source terms or any external forces to the right-hand side of the equations. However, we are more interested in fluid with an external forces such as the gravity force or any radiative forces which will allow the gas to leave the star to the interstellar medium, as in our case, the stellar winds of massive stars.

2.2 1D Spherically symmetric wind

The hydrodynamic model of stellar winds is expressed in spherical geometry (r,θ,ϕ), and assuming axial symmetry,y can be written as (Bjorkman and Cassinelli, 1993; Owocki, Cranmer, and Blondin, 1994; Cranmer, 1996):

$$
\begin{aligned}
\frac{\partial \rho}{\partial t}+\frac{1}{r^2}\frac{\partial(r^2\rho v_r)}{\partial r}+\frac{1}{r\sin\theta}\frac{\partial(\rho v_\theta \sin\theta)}{\partial \theta} &= 0,\\
\frac{\partial v_r}{\partial t}+v_r\frac{\partial v_r}{\partial r}+\frac{v_\theta}{r}\frac{\partial v_r}{\partial \theta}-\frac{v_\theta^2+v_\phi^2}{r} &= -\frac{1}{\rho}\frac{\partial P}{\partial r}+g_r^{\mathrm{ext}},\\
\frac{\partial v_\theta}{\partial t}+v_r\frac{\partial v_\theta}{\partial r}+\frac{v_\theta}{r}\frac{\partial v_\theta}{\partial \theta}-\cot\theta\frac{v_\theta^2}{r}+\frac{v_r v_\theta}{r} &= -\frac{1}{r\rho}\frac{\partial P}{\partial \theta}+g_\theta^{\mathrm{ext}},\\
\frac{\partial v_\phi}{\partial t}+v_r\frac{\partial v_\phi}{\partial r}+\frac{v_\theta}{r}\frac{\partial v_\phi}{\partial \theta}+\cot\theta\frac{v_\theta^2}{r}+\frac{v_r v_\phi}{r} &= g_\phi^{\mathrm{ext}},\\
P &= a^2\rho, \qquad (2.5)
\end{aligned}
$$

where v_r, v_θ, v_ϕ are the velocity components in every direction, and a is the isothermal sound speed. The external force $\boldsymbol{g}^{ext}$ is the sum of the gravitation and the CAK line driving force.

Consider a one-dimensional steady state, and spherically symmetric wind, of a star with mass $M_\star$, radius $R_\star$, and mass loss rate $\dot{M}$. The mass conservation equation reduces to (Cranmer, 1996; Lamers and Cassinelli, 1999)

$$\frac{1}{r^2}\frac{d}{dr}(\rho v_r r^2)=0, \qquad (2.6)$$

integrating this gives the mass loss per unit of time;

$$\dot{M}=4\pi\rho v_r r^2=\text{constant}. \qquad (2.7)$$

The momentum equation can be given by

$$v_r\frac{dv_r}{dr}=-\frac{1}{\rho}\frac{\partial P}{dr}+g_r. \qquad (2.8)$$

Using the equation of state of an ideal gas, the pressure can be expressed as $P=\rho a^2$. We can now replace the gradient in the continuity equation (2.6) to get,

$$\frac{1}{\rho}\frac{dP}{dr}=a^2\frac{1}{\rho}\frac{d\rho}{dr}=-\frac{a^2}{v}\frac{dv}{dr}-\frac{2a^2}{r}. \qquad (2.9)$$

Substituting into (2.8) yields:

$$(v^2-a^2)\frac{1}{v}\frac{dv}{dr}=\frac{2a^2}{r}-\frac{da^2}{dr}+g_r, \qquad (2.10)$$

where g_r is the external radial force, which can be written in terms of gravitational and radiation forces, where the latter can be separated into that due to the continuum and spectral lines,

$$g_r=-\frac{GM_\star}{r^2}+g_{rad}^C+g_{rad}^L. \qquad (2.11)$$

Here we will consider only the gravity force and we will consider the radiative force in the following section. Plugging the expression of g_r into (2.10) we get,

$$(v^2 - a^2)\frac{1}{v}\frac{dv}{dr} = \frac{2a^2}{r} - \frac{GM_\star}{r^2}. \tag{2.12}$$

When the left-hand side vanishes, we obtain the critical radius r_c which gives the critical solution, where

$$r_c = \frac{GM_\star}{2a^2}. \tag{2.13}$$

To satisfy the isothermal wind assumption, the critical point (r_c) should be larger than the initial radius (r_0) , otherwise there will be no isothermal regime. The velocity gradient at the critical distance will vanish because the numerator is zero, unless $v(r_c) = a$. Similarly, the gradient of the velocity will be $\pm\infty$ at the distance where $v = a$, because the denominator is zero, unless $r = r_c$.

The topology of the solution of Eq 2.12 is illustrated in Fig 2.1 (Lamers and Cassinelli, 1999). From the figure, we can observe multiple solutions, each with its specific set of boundary conditions. The majority of these solutions are without physical significance, despite being mathematically acceptable. For example, solutions 4 and 6 can be excluded because there is no observational evidence of solar corona which starts supersonically at the base. Solution 3 is called stellar "breeze", where the wind speed has zero asymptotes leading to finite pressure at larger radii, which do not match with the pressure of the interstellar medium. Solution 2 is called Boundi accretion because it starts supersonic and goes to subsonic, with negative velocity. The most acceptable solution is type 1 where the wind starts subsonic passing through the critical point and expands to supersonic.

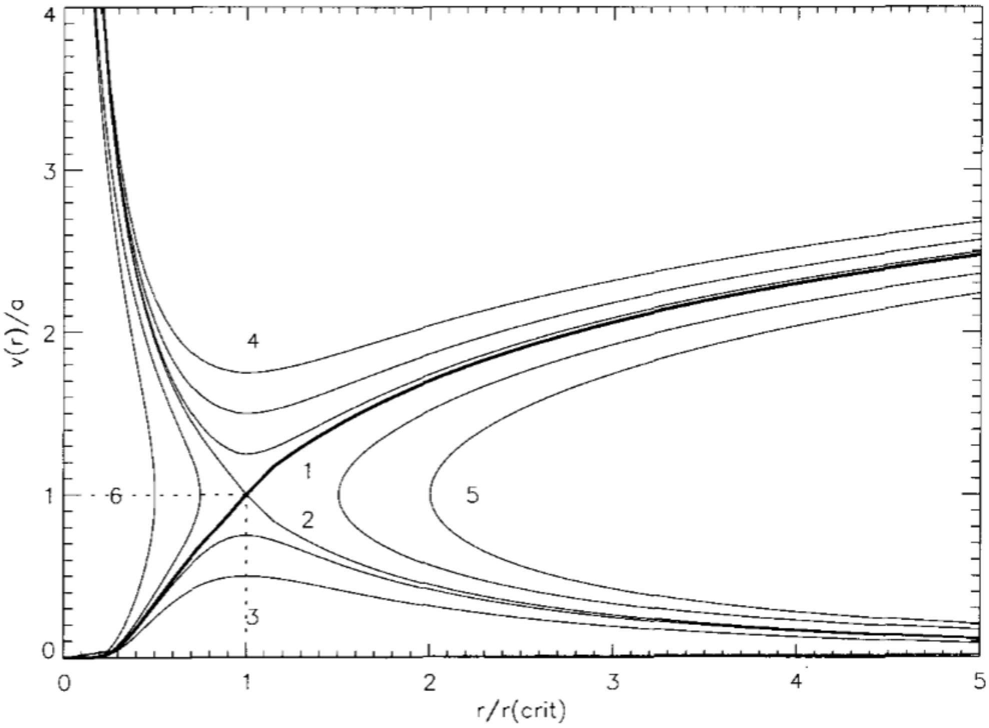

Figure 2.1: Solution of isothermal stellar wind momentum equation (Lamers and Cassinelli, 1999).

2.3 The Sobolev approximation

Most massive stars have high temperatures and high luminosity, leading to strong stellar winds, which impact the interstellar medium and the evolution of these stars. The solar wind is driven by gas pressure gradient, however, the hot star winds are driven by radiative pressure gradient.

The force per unit mass due to the radiation (Cranmer and Owocki, 1995; Cranmer, 1996; ud-Doula, 2002) is given by:

$$\boldsymbol{g}_{\rm rad} = \frac{1}{c}\oint\int_{\nu=0}^{\infty}\kappa_\nu I_\nu(\boldsymbol{r},\boldsymbol{n})\boldsymbol{n}d\Omega d\nu, \tag{2.14}$$

where κ_ν is the total mass extinction coefficient which includes absorption and scattering. I_ν is the monochromatic radiative intensity along the direction $\boldsymbol{n}$.

Neglecting free-free and bound-free absorption, the total mass extinction can be expressed in two terms as:

$$\kappa_\nu = \kappa_e + \kappa_L, \tag{2.15}$$

where κ_e is the mass absorption coefficient due to electron scattering, and κ_L the absorption coefficient due to bound electrons of line. Hence, the radiation force can be expressed in terms of two forces, one due to electrons scattering g_e and the other due to line g_L:

$$\boldsymbol{g}_{\rm rad} = \boldsymbol{g}_e + \boldsymbol{g}_L. \tag{2.16}$$

2.3.1 Force due to electron scattering

For an optically thin wind (such as in O and B stars), the scattering caused by free electrons can be taken into account, leading to the expression of radiative acceleration (Cranmer and Owocki, 1995; Owocki, 2013)

$$\boldsymbol{g}_e = \frac{\kappa_e}{c} \oint I_\nu(\boldsymbol{r}, \boldsymbol{n}) \boldsymbol{n} d\Omega. \tag{2.17}$$

Assuming a point source star in spherical geometry, the integrand of Eq 2.17 gives the total radiation flux and the force, in optical thin wind can be written as

$$g_e = \frac{\kappa_e}{c} \frac{L_\star}{4\pi r^2}, \tag{2.18}$$

where $L_\star$ is the luminosity of the star. As can be seen that the force is inversely proportional to r^2, therefore we can compare it to the gravity force, by defining the Eddington parameter as;

$$\Gamma_\mathrm{E} \equiv \frac{g_e}{g} = \frac{\kappa_e L_\star}{4\pi G M_\star c}. \tag{2.19}$$

The ratio, commonly referred to as the Eddington parameter, possesses a distinct value for each star. In the case of the Sun, this value is exceedingly small, about 2.10^{-5}. However, for hot, massive stars, it has the potential to approach unity. As Eddington observed, electron scattering leads to a fundamental radiative acceleration that effectively counters the gravitational forces exerted by the star. When the limit $\Gamma_\mathrm{E} \to 1$ is reached, this is known as the Eddington limit, indicating that the star would no longer be gravitationally bound (Owocki, 2013).

2.3.2 Line force of single line

The line force can be expressed as (Cranmer and Owocki, 1995; Cranmer, 1996; ud-Doula, 2002):

$$\boldsymbol{g}_L = \frac{\kappa_L}{c} \oint \int_{\nu=0}^{\infty} \phi(\nu - \nu') I_\nu(\boldsymbol{r}, \boldsymbol{n}) \boldsymbol{n} d\Omega d\nu, \tag{2.20}$$

where $\phi(\nu)$ is the normalized line profile function, ν' is the frequency of the line in the comoving frame of the gas related to the emitted frequency ν_0 by

$$\nu' = \nu_0 \left(1 + \frac{\boldsymbol{n}.\boldsymbol{v}(\boldsymbol{r})}{c}\right), \tag{2.21}$$

in non-relativistic domain and $\boldsymbol{v}(\boldsymbol{r})$ is the velocity of the flow. A change of variables can be introduced and the frequency can be defined in terms of Doppler widths as

$$x = \frac{\nu - \nu_0}{\Delta\nu_D}. \tag{2.22}$$

The line force can be rewritten as:

$$\boldsymbol{g}_L = \frac{\kappa_L \Delta\nu_D}{c} \oint \int_{-\infty}^{\infty} \phi\left(x - \frac{\boldsymbol{n}.\boldsymbol{v}(\boldsymbol{r})}{v_{th}}\right) I_\nu(\boldsymbol{r}, \boldsymbol{n}) \boldsymbol{n} d\Omega dx, \tag{2.23}$$

where the Doppler width is $\Delta\nu_D = \nu_0 v_{th}/c$, with ion thermal speed v_{th}. The lower limit of the integral of x is extended from $-c/v_{th}$ to $-\infty$ with a negligible error.

For optically thin wind to continuum radiation, the continuum integral is simply the bolometric flux $F_\star$ (Eq 2.17), however for the lines, the integral is more complicated. The general, time independent radiative transfer equation is given by (Cranmer, 1996)

$$\frac{dI_\nu}{d\tau_\nu} = -I_\nu + S_\nu; \tag{2.24}$$

the formal solution is

$$I_\nu(\tau_\nu) = I_\nu^0 e^{-\tau_\nu} + \int_0^{\tau_\nu} S_\nu(t_\nu) e^{-(\tau_\nu - t_\nu)} dt_\nu, \tag{2.25}$$

where $S_\nu(\tau_\nu)$ is the source function of the medium, and the optical depth τ_ν is defined along general path length s, as

$$\tau_\nu = \int_0^s \kappa_L \rho(s') \phi\left(x - \frac{\boldsymbol{n}.\boldsymbol{v}(\boldsymbol{r})}{v_{\rm th}}\right) ds'. \tag{2.26}$$

For isotropic emission, we can take only the term $I_\nu^\star e^{-\tau}$, where the superscript $\star$ stands for the radiation from the star, from the formal solution of the intensity, the radiative force can be written as

$$\boldsymbol{g}_{\rm rad} = \frac{\sigma_e \boldsymbol{F}_\star}{c} + \sum_{\rm lines} \frac{\kappa_L \Delta\nu_D}{c} \oint \int_{-\infty}^{+\infty} \phi\left(x - \frac{\boldsymbol{n}.\boldsymbol{v}(\boldsymbol{r})}{v_{\rm th}}\right) I_\nu^\star e^{-\tau_\nu} \boldsymbol{n} d\Omega dx; \tag{2.27}$$

in a wind characterized by a steadily increasing velocity, it is possible to simplify the integral for optical depth (Eq 2.26) by utilizing the Sobolev approximation (Cranmer, 1996). This approximation assumes that the variables κ_L and ρ do not experience significant changes over a distance known as the " Sobolev length" L_S. When the fluid velocity is sufficiently high, the dominant factor in the integrand is the Doppler shift of the line frequency, line profile function ϕ becomes sharply peaked as a function of r, where the frequency x resonates with the local component of the fluid velocity. We can take out the variable κ_L and ρ, so the optical depth can be written as

$$\tau_\nu(r) = \kappa_L \rho(r) \int_0^s \phi\left(x - \frac{\boldsymbol{n}.\boldsymbol{v}(\boldsymbol{r}')}{v_{\rm th}}\right) ds'. \tag{2.28}$$

The path length extends from the surface of the star located at the position vector $\boldsymbol{r}_0$ to the "observer" situated in the wind at position vector r, where the value of s' varies from 0 to s. The current position $\boldsymbol{r}'$ can be expressed as the sum of $\boldsymbol{r}_0$ and s' times the unit vector $\boldsymbol{n}$. Due to the assumption of a monotonic flow, it is possible to transform the variables into frequency space so that

$$x' = x - \frac{\boldsymbol{n}.\boldsymbol{v}(\boldsymbol{r}')}{v_{\rm th}} \tag{2.29}$$

$$dx' = -\frac{1}{v_{\rm th}} d[\boldsymbol{n}.\boldsymbol{v}(\boldsymbol{r}')] = -\frac{1}{v_{\rm th}} \boldsymbol{n}.\nabla[\boldsymbol{n}.\boldsymbol{v}(r')] ds', \tag{2.30}$$

and this gives

$$\tau_\nu = \frac{\kappa_L v_{\rm th}\rho(r)}{(\boldsymbol{n}.\nabla)(\boldsymbol{n}.\boldsymbol{v}(r))}\int_{x-\frac{\boldsymbol{n}.\boldsymbol{v}(r)}{v_{\rm th}}}^{\infty}\phi(x')dx'. \tag{2.31}$$

The constant part can be defined as Sobolev optical depth

$$\tau_S \equiv \frac{\kappa_L v_{\rm th}\rho(r)}{(\boldsymbol{n}.\nabla)(\boldsymbol{n}.\boldsymbol{v}(r))} = \kappa_L\rho(r)L_S, \tag{2.32}$$

and the integral part

$$\Phi(x,r) \equiv \int_{x-\frac{\boldsymbol{n}.\boldsymbol{v}(r)}{v_{\rm th}}}^{\infty}\phi(x')dx'. \tag{2.33}$$

We can now write the force for the single line as

$$\boldsymbol{g}_L = \frac{\kappa_L\Delta\nu_D}{c}\oint\int_{-\infty}^{+\infty}\phi(x')\,I_\nu^\star\,e^{-\tau_S\,\Phi(x',r)}\boldsymbol{n}d\Omega dx' \tag{2.34}$$

$$= \frac{\kappa_L\Delta\nu_D}{c}\oint\int_{-\infty}^{+\infty}I_\nu^\star\,e^{-\tau_S\,\Phi(x',r)}\boldsymbol{n}d\Omega d\Phi(x',r), \tag{2.35}$$

integrating this equation gives

$$\boldsymbol{g}_L = \frac{\kappa_L\Delta\nu_D}{c}\left(\oint I_\nu^\star\boldsymbol{n}d\Omega\left[\frac{1-e^{-\tau_S}}{\tau_S}\right]\right). \tag{2.36}$$

For a point source star, the term in the bracket is the total radiation flux at distance r and frequency ν, and the radial component of the force becomes

$$g_L = \frac{\kappa_L\nu_0 L_\nu v_{\rm th}}{4\pi r^2 c^2}\left[\frac{1-e^{-\tau_S}}{\tau_S}\right], \tag{2.37}$$

and the Sobolev optical depth

$$\tau_S \equiv \frac{\kappa_L v_{\rm th}\rho(r)}{\partial v_r/\partial r}. \tag{2.38}$$

In massive stars, the flux at the position of lines can be roughly approximated by $\nu_0 L_\nu \approx L_\star$, so

$$g_L = \frac{\kappa_L L_\star v_{\rm th}}{4\pi r^2 c^2}\left[\frac{1-e^{-\tau_S}}{\tau_S}\right]. \tag{2.39}$$

For optically thin medium $\tau_S \ll 1$, so the term $1-e^{-\tau_S} \approx 1$, and for optical thick medium $\tau_S \gg 1$ the exponential term $e^{-\tau_S}$ becomes negligible, and

$$g_L = \frac{1}{\rho c^2}\frac{L_\star}{4\pi r^2}\frac{\partial v_r}{\partial r}. \tag{2.40}$$

In this section, we showed the formulation of radiation force due to a single line in the stellar wind. However, the total radiative force is due to a large number of lines we show next the total force for an ensemble of lines.

2.3.3 Force for an ensemble of lines

The production of radiative acceleration in a stellar wind is caused by a diverse set of lines with varying optical depth. The Collective effect of these individual lines contributes to the total line radiative acceleration, which is calculated by summing the contributions of each line (ud-Doula, 2002)

$$g_{\text{lines}} = \sum_{\text{lines}} \frac{\kappa_L v_{\text{th}}}{c^2} \frac{L_\star}{4\pi r^2} \left[\frac{1 - e^{-\tau_S}}{\tau_S} \right]. \tag{2.41}$$

In reality, the number of lines is huge and can be described by the statistical distribution. CAK introduced the dimensionless optical depth

$$t \equiv \frac{\sigma_e \rho v_{\text{th}}}{dv/dr}, \tag{2.42}$$

and parametrized the line acceleration as:

$$g^L_{\text{rad}} \propto k t^{-\alpha}, \tag{2.43}$$

where σ_e is the value for the electron scattering cross-section, k defines the line force strength, α determines the importance of optically thin and thick lines in the distribution; for thin lines $\alpha = 0$, and for thick lines $\alpha = 1$. Following the CAK work, further modification by Owocki, Castor, and Rybicki (1988)(OCR) to approximate the number distribution of lines as an exponentially-truncated power law;

$$\frac{dN(\kappa)}{d\kappa} = \frac{1}{\kappa_0} \left(\frac{\kappa_L}{\kappa_0} \right)^{\alpha-2} e^{-\kappa/\kappa_{max}}, \tag{2.44}$$

where κ_0 is the normalization factor that is associated with CAK parameter k, and is given by $\kappa_0 = \Gamma(\alpha)(v_{\text{th}}/c)(\kappa_0/\kappa_e)^{1-\alpha}/(1-\alpha)$, κ_{max} is the cutoff which limits the maximum line strength (OCR), and $\Gamma(\alpha)$ is the Gamma function. With this formulation the sum over lines in the force is replaced by an integral (Puls, Springmann, and Lennon, 2000)

$$\sum_{\text{lines}} g^L_{\text{rad}} \approx \int_0^\infty g^L_{\text{rad}} \frac{dN}{d\kappa_L} d\kappa_L, \tag{2.45}$$

and the total force becomes

$$g_{\text{lines}} = \int_0^\infty \frac{\kappa_L v_{\text{th}}}{c^2} \frac{L_\star}{4\pi r^2} \left[\frac{1 - e^{-\tau_S}}{\tau_S} \right] \frac{1}{\kappa_0} \left(\frac{\kappa_L}{\kappa_0} \right)^{\alpha-2} e^{-\kappa/\kappa_{max}} d\kappa_L. \tag{2.46}$$

This can be easily integrated by letting $\kappa_{max} \to \infty$.

In his paper, Gayley (1995) introduced a new formulation of the CAK line force by introducing $\bar{Q}$, a quantity that is closely linked to the classical oscillator strength. This formulation effectively removes the dependence on the thermal velocity (vth) from the equation. Gayley assumes that the following identity holds

$$\frac{\kappa_0 v_{\text{th}}}{c} \equiv \bar{Q} \kappa_e \Gamma(\alpha)^{-\frac{1}{1-\alpha}}. \tag{2.47}$$

The line force can be written as

$$g_{\text{lines}} = \frac{1}{1-\alpha} \frac{\bar{Q} \kappa_e L_\star}{4\pi r^2 c} \left(\frac{\partial v/\partial r}{\rho c \bar{Q} \kappa_e} \right)^\alpha . \tag{2.48}$$

2.3.4 Solution in 1-D

In massive stars' wind, the line force is dominant, and the gas pressure the gradient is negligible; the momentum equation in 1-D steady state, in spherical geometry can be written as (Cranmer, 1996; Lamers and Cassinelli, 1999; ud-Doula, 2002; Owocki, 2013):

$$v\frac{dv}{dr} = -\frac{GM_\star(1-\Gamma_e)}{r^2} + g_{\text{lines}}. \tag{2.49}$$

Gravity moderates the feedback between line driving and flow acceleration. We define gravitationally scaled inertial acceleration as follows (Cranmer, 1996; Lamers and Cassinelli, 1999; ud-Doula, 2002; Owocki, 2013):

$$W \equiv \frac{r^2 v dv/dr}{GM_\star(1-\Gamma_e)}, \tag{2.50}$$

thus

$$CW^\alpha = 1 + W, \tag{2.51}$$

where the constant $C \propto 1/\dot{M}^\alpha$ determines the mass loss rate. Figure 2.2 shows the graphical solution of the Eq 2.51 for different values of C. In this equation, the left-hand side represents the line force, while the right-hand side tells us how much of that force is attributed to inertia (W) and gravity. If the mass flow rate, represented by $\dot{M}$, is high or if C is small, there are no solutions. Conversely, if the mass flow rate is small or C is high, there are two solutions. The critical solution, located between these two extremes, corresponds to the maximum CAK mass loss rate solution. To achieve this solution, the CW^α line and the $1+W$ line must intersect tangentially, this implies

$$C_c \alpha W^{\alpha-1} = 1, \tag{2.52}$$

solving for W, we obtain,

$$W = \frac{\alpha}{1-\alpha} = \text{constant}. \tag{2.53}$$

The critical value C_c is given by

$$C_c = \frac{(1-\alpha)^{\alpha-1}}{\alpha^\alpha}, \tag{2.54}$$

replacing the constant C and after some manipulations, we can find

$$\dot{M}_{\text{CAK}} = \frac{L_\star}{c^2}\frac{\alpha}{1-\alpha}\left[\frac{\bar{Q}\Gamma_e}{1-\Gamma_e}\right]^{(1-\alpha)/\alpha}. \tag{2.55}$$

Integrating the critical acceleration ω_c from the surface radius R, we obtain the general beta velocity law

$$v(r) = v_\infty\left(1 - \frac{R_\star}{r}\right)^\beta \tag{2.56}$$

For $\beta = 1/2$, we find the wind terminal speed

$$v_\infty = v_{\text{esc}}\sqrt{\frac{\alpha(1-\Gamma_e)}{1-\alpha}}, \tag{2.57}$$

where $v_{\rm esc} = \sqrt{2GM(1-\Gamma_e)/R_\star}$ is the escape velocity from the stellar surface.

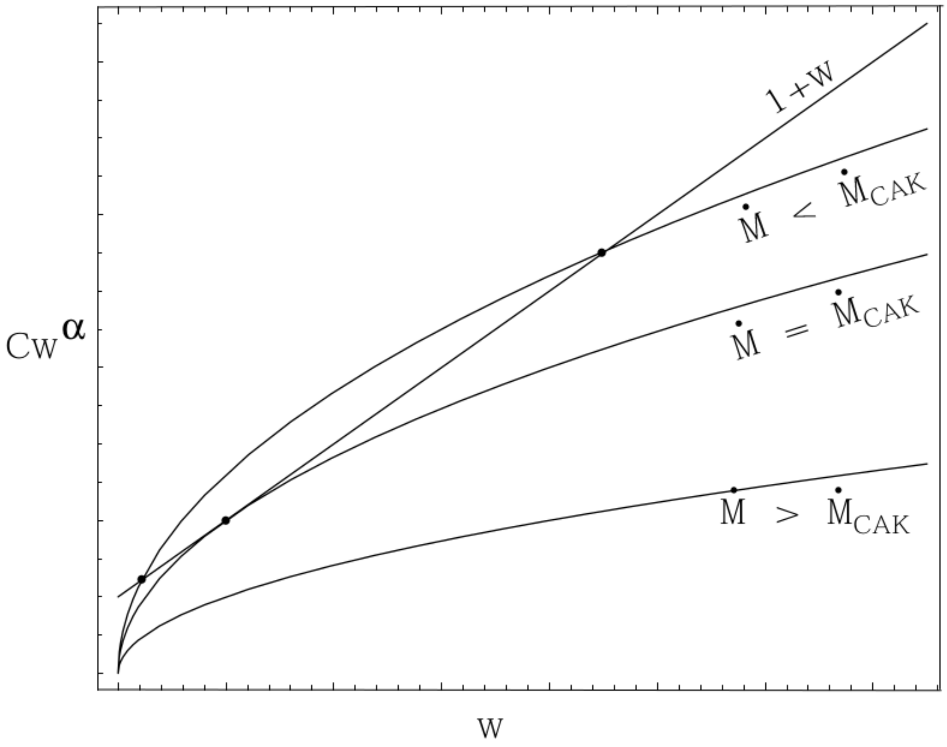

Figure 2.2: Graphical solution of 1D CAK wind model (ud-Doula, 2002)

These results apply to an ideal assumption that the radiation is illuminated from a point source. The derived expressions of the mass loss rate and the terminal velocity were obtained by neglecting the gas pressure term in the momentum equation. Including the gas pressure and solving the full momentum equation can lead to similar expressions of the mass loss rate and the terminal velocity, a detailed analysis can be found in the book of Lamers and Cassinelli (1999).

Despite the aforementioned complexities of the line force, the Sobolev approach appears suitable for modeling the dynamic of wind of massive stars in optical thin stellar wind. However, the model of CAK line force breaks down in the optically thick wind, and as discussed in the recent work by Sundqvist et al. (2019), the occurrence of overlap of close to the star the lines lead to the escape of radiation, thus reducing acceleration and creating difficulties in explaining high mass-loss rates of WR stars. To solve these difficulties, Moens et al. (2022) developed multidimensional radiation modules based on flux-limited diffusion approximation. They found a smooth transition from the dense outflows of traditional WR stars to the less dense winds of smaller, hotter subdwarf stars (Vink et al., 2011). This shift occurs at a luminosity level that is roughly 40 % of the Eddington luminosity.

Chapter 3

Rapid stellar rotation

Modeling stars requires a multidimensional approach, but many stars, especially intermediate and high-mass stars, are known to be fast rotators (Owocki, Cranmer, and Blondin, 1994; Huang, Gies, and McSwain, 2010), which disrupts their spherical symmetry. The distorted stellar surface causes the variation of surface brightness and the variation of the effective temperature, which has been observed interferometrically for a number of stars (van Belle et al., 2001; Che et al., 2011).

In this chapter, we briefly show the standard Roche model commonly used to model the rapid rotators. The assumptions of the Roche model shown by Cranmer and Owocki (1995) as a point mass with uniform rotation concentrated in the center of the star. To describe the temperature variation along stellar surface we combine Roche model with von Zeipel's theorem.

3.1 Shape of rotating stars

Rotation plays a crucial role in the evolution of stars, particularly hot massive ones. The fast rotation of these stars can lead to the shedding of their outer envelope, causing changes in their shape. The shape of a star is determined by its stellar radius, which varies with different angles of co-latitude (θ) within the star. This rotational phenomenon is especially significant for massive stars and affects their evolution in a notable way (Cranmer, 1996; Maeder, 2009).

The superposition of gravitational potential and the centrifugal term of point source with mass $M_\star$ is given by

$$\Phi(r,\theta) = -\frac{GM_\star}{r} - \frac{1}{2}\Omega^2 r^2 \sin^2\theta, \tag{3.1}$$

where Ω is the angular velocity of the body. This is called Roche model of the solid body, the inner layers are considered spherical and not distorted by rotation. At the pole, the centrifugal term vanishes ($r = R_p, \theta = 0$); the potential at the pole is compared to the one at any θ, for $r = R(\theta)$

$$\frac{GM_\star}{R_p} = \frac{GM_\star}{R} + \frac{1}{2}\Omega^2 R^2 \sin^2\theta. \tag{3.2}$$

The shape of the Roche model is shown in Fig 3.1 for different rotational velocities.

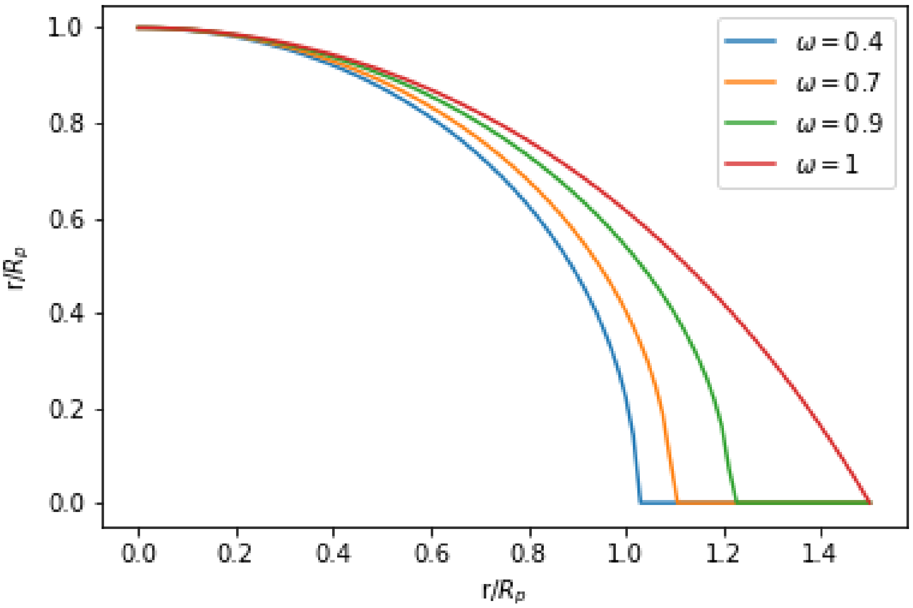

Figure 3.1: Shapes of fast rotating stars for different rotational velocities

The resulting effective gravity from the gradient of gravitational and centrifugal potentials is given by (Maeder, 2009),

$$\vec{g}_{\text{eff}} = \left[-\frac{GM_\star}{R^2} + \Omega^2 R \sin^2\theta \right] \vec{e_r} + \left[\Omega^2 R \sin\theta \cos\theta \right] \vec{e_\theta}, \tag{3.3}$$

and the magnitude of the effective gravity is $g_{\text{eff}} = |\vec{g}_{\text{eff}}|$,

$$g_{\text{eff}} = \sqrt{\left[-\frac{GM_\star}{R^2} + \Omega^2 R \sin^2\theta \right]^2 + \Omega^4 R^2 \sin^2\theta \cos^2\theta}. \tag{3.4}$$

Figure 3.2 shows the variation of the effective gravity, scaled by polar gravity, as a function of co-latitude θ for different rotation velocities.

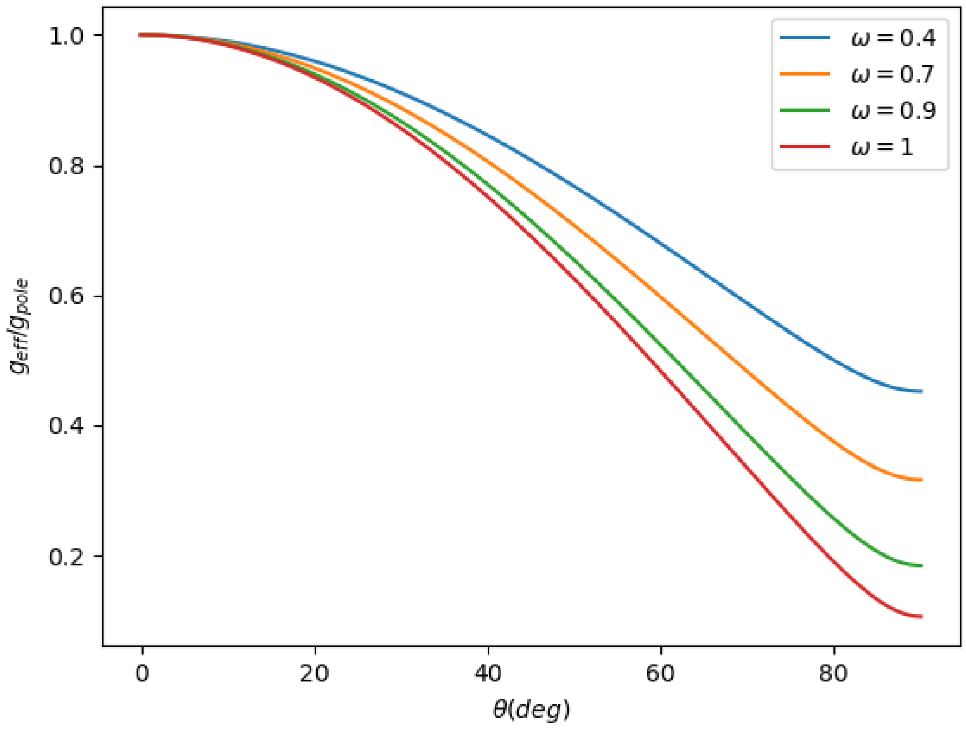

Figure 3.2: Surface gravity of rotating stars as a function of colatitude.

3.2 Critical velocity

To reach the critical velocity, the centrifugal force should equate the gravity (Maeder, 2009). The maximum angular velocity, where $g_{\rm eff} = 0$, at the equator ($\theta = \pi/2$), is given by

$$\Omega^2_{\rm crit} = \frac{GM_\star}{R^3_{\rm eq,crit}}, \tag{3.5}$$

where $R_{\rm eq,crit}$ is the equatorial radius at the critical rotation, replacing the value of $\Omega_{\rm crit}$ in Eq 3.2 we can get the ratio of the equatorial to polar radius at the critical velocity

$$\frac{R_{\rm eq,crit}}{R_{\rm p,crit}} = \frac{3}{2}, \tag{3.6}$$

Introducing the non-dimensional rotation parameter ω as the ratio between the angular velocity to the angular velocity at the critical rotation,

$$\omega = \frac{\Omega}{\Omega_{\rm crit}} = \left[\frac{\Omega^2 R^3_{\rm eq,crit}}{GM_\star}\right]^{\frac{1}{2}}, \tag{3.7}$$

and for $x = R/R_{\mathrm{p}}$, Eq 3.2 becomes

$$\frac{1}{x} + \frac{4}{27}\omega^2 x^2 \sin^2\theta = 1. \tag{3.8}$$

This is the cubic equation, and the shape of the stellar surface (Collins, 1963; Owocki, Cranmer, and Blondin, 1994; van Belle et al., 2001) is given by

$$x(\theta,\omega) = \frac{3}{\omega \sin\theta} \cos\left(\frac{\pi + \arccos(\omega \sin\theta)}{3}\right). \tag{3.9}$$

3.3 Theorem of von Zeipel

In 1924, von Zeipel showed that the distorted hydrostatic equilibrium of the star impacts the net radiative flux, which is proportional to local gravity over its surface. The gravity darkening can be expressed by assuming a hydrostatic equilibrium of the star's interior where the effective gravity $\boldsymbol{g}_{\mathrm{eff}}$ is derived from effective potential Φ (Cranmer, 1996; Maeder, 2009)

$$\nabla P = \rho \boldsymbol{g}_{\mathrm{eff}} = -\rho \nabla \Phi \tag{3.10}$$

The gradient of pressure P and the normal to the potential surfaces are anti-parallel, and this imposes that the gas pressure should be constant on the equipotential surfaces, which results in P must be a function of Φ only, where the density can be expressed as

$$\rho = \frac{|\nabla P(\Phi)|}{|\nabla \Phi|} = -\frac{dP}{d\Phi}, \tag{3.11}$$

thus the density also is a function of Φ. In radiative equilibrium, the flux carried outward by photons is proportional to the conductive term,

$$\mathcal{F} = -\frac{16\sigma_B}{3\kappa\rho} T^3 \nabla T, \tag{3.12}$$

where κ is the Rosseland mean absorption coefficient and σ_B is the Stefan-Boltzmann constant. We can write

$$\nabla T = \frac{dT}{d\Phi} \nabla \Phi. \tag{3.13}$$

The flux of a rotating star can be written as

$$\mathcal{F} = -f(r,\theta) \boldsymbol{g}_{\mathrm{eff}}, \tag{3.14}$$

where $f(r,\theta)$ is a function to be determined.

The variation of the effective temperature T_{eff}, over the surface of a rotating star, with local gravity, is given by the gravity darkening law, introduced by von Zeipel (1924)

$$T_{\mathrm{eff}} = \frac{K}{\sigma_B} g_{\mathrm{eff}}^{0.25}, \tag{3.15}$$

where K is the von Zeipel constant given by the condition that the total integral of the flux gives the luminosity of the star $L_\star$ regardless of the degree of rotation. The constant K is given by

$$K = \frac{L_\star}{\oint g_{\text{eff}}.dS}, \tag{3.16}$$

where the denominator is integrated over the entire surface of the star, the integrand was shown by Cranmer and Owocki (1995) to be proportional to the even powers of ω.

3.4 Espinosa Lara and Rieutord formulation

The formulation of von Zeipel does not take into account the convection and it neglects the Eddington-Sweet current; 2D simulation using ESTER code by Rieutord and Espinosa Lara (2009) showed the difference between von Zeipel law and numerical model with gravity darkening. Following this work Espinosa Lara and Rieutord (2011) have improved the gravity darkening equation to take into account fast rotation. The formulation started by letting $\mathcal{F} = f(r,\theta)\boldsymbol{g}_{\text{eff}}$, and imposing the condition $\nabla\mathcal{F} = 0$ to determine the unknown function $f(r,\theta)$. Using the solid body rotation of Roche model the cubic equation 3.9 was modified, and expressed in terms of Θ rather than x, as follows

$$\cos\Theta + \ln\left(\tan\frac{\Theta}{2}\right) = \frac{1}{3}x^3\omega^2\cos^3\theta + \cos\theta + \ln\left(\tan\frac{\theta}{2}\right), \tag{3.17}$$

and this led to the new expression of the effective temperature, as

$$T_{\text{eff}} = \left(\frac{L_\omega}{\sigma_B G M_\star}\right)^{1/4}\sqrt{\frac{\tan\Theta}{\tan\theta}}\, g_{\text{eff}}^{1/4}, \tag{3.18}$$

after substitution, we can express the equatorial to polar effective temperature, as follows:

$$T^{\text{e}}_{\text{eff}} = T^{\text{p}}_{\text{eff}}\sqrt{\frac{2}{2+\omega^2}}\left(1-\omega^2\right)^{1/12}\exp\left(-\frac{4\omega^2}{(6+3\omega^2)^3}\right), \tag{3.19}$$

from which we can recover von Zeipel's theorem at slow rotation

$$T_{\text{eff}} = \left(\frac{L}{4\pi\sigma_B G M}\right)^{\frac{1}{4}} g_{\text{eff}}^{\frac{1}{4}}. \tag{3.20}$$

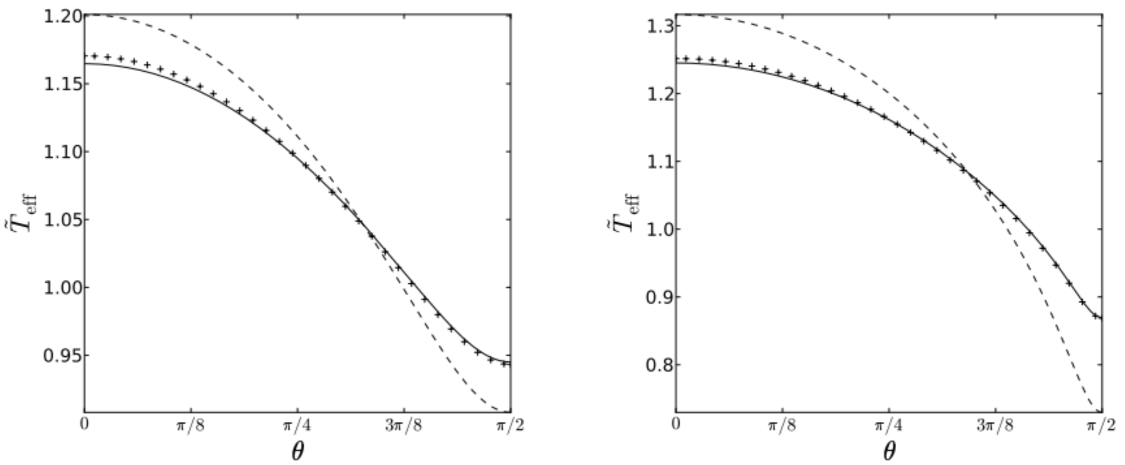

Figure 3.3: Comparison between gravity darkening computed using von Zeipel's law (dashed line), Espinosa's model (solid line), and model using 2D ESTER code (crosses). Left with rotation rate $\omega = 0.7$ and right with rotation $\omega = 0.9$ (Espinosa Lara and Rieutord, 2011).

A comparison between the model of Espinosa Lara and von Zeipel's theorem is shown in Fig 3.3, it is clear from the plot that a good agreement was found between the 2D ESTER code and the formulation by Espinosa Lara. Figure 3.4 shows the distribution of the effective temperature, projected in the XZ plane, where $\tilde{x}$ and $\tilde{z}$ are the Cartesian coordinate (x,z) scaled by Keplerian radius a.

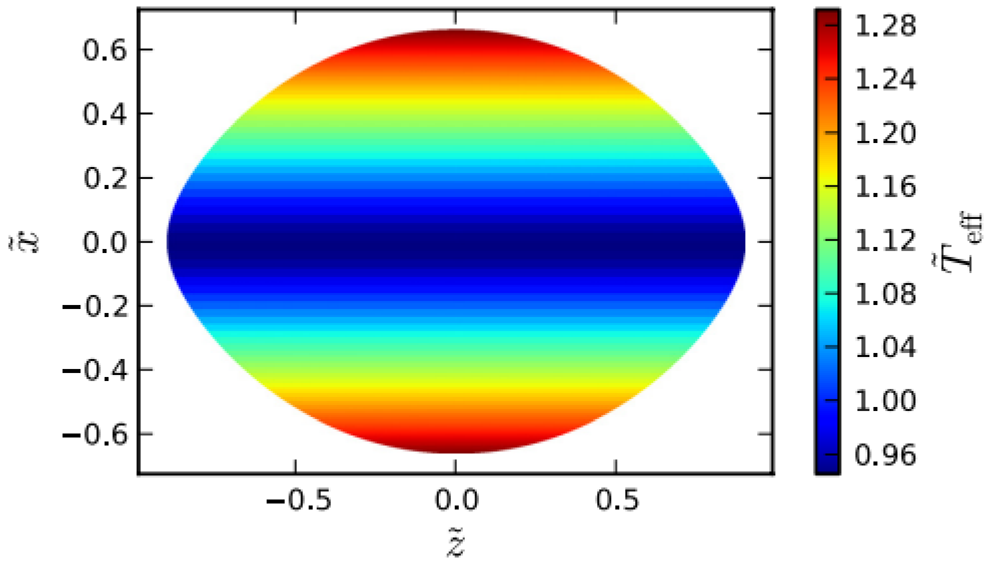

Figure 3.4: Variation of the effective temperature, where $\tilde{T}_{\rm eff}$ is the normalized value defined as $T_{\rm eff}(\frac{L}{4\pi\sigma R_e^2})^{-1/4}$ (Espinosa Lara and Rieutord, 2012).

Stars that rotate rapidly undergo significant distortions due to their non-spherical shape. As initially demonstrated by von Zeipel (1924), the emission of radiation from a rotating star is not evenly distributed across its surface. This principle, known as the von Zeipel theorem, states that the radiative flux is greater in the polar regions compared to the equatorial regions, as the effective gravitational force is stronger at the poles. Consequently, this results in a phenomenon known as "gravity darkening," where the equatorial regions appear darker than the polar caps. Numerous observations have extensively confirmed the existence of this phenomenon (e.g, Domiciano de Souza et al., 2014). The redistribution of flux caused by this effect has significant implications, including the modification of inferred fundamental properties such as effective temperatures (Espinosa Lara and Rieutord, 2011). Therefore, the rapid rotation of stars affects their structure and evolution through both centrifugal distortion and the effects of gravity darkening.

Chapter 4

Radiative transfer and polarization

In the previous chapter, we showed the effects of fast stellar rotation and how it could distort the geometry of the stars, leading to an oblate structure of the equipotential surface, known as the gravity-darkening model. The rotation does not impact only the structure, but also the physics. Because of the change in the sphericity, this leads to the occurrence of electron scattering in media that is not spherically symmetric, which will result in an intrinsic polarization; in this chapter, we will show how the radiation will be transferred. We will mainly focus on the polarization due to electron scattering in the wind.

4.1 Unpolarized radiation

The general time-independent radiative transfer equation is a mathematical expression that describes the behavior of radiation as it interacts with a medium, and can be expressed as (Chandrasekhar, 1960; Hubeny and Mihalas, 2015)

$$\frac{dI_\nu}{ds} = -\kappa_\nu \rho I_\nu + j_\nu \rho, \tag{4.1}$$

where κ_ν is the absorption coefficient, j_ν is the emission coefficient for the radiation with the frequency ν, ρ is the density of the material crossed by the radiation, I_ν is the specific intensity, which depends on the frequency and the direction of radiation, so that the radiation flux is written as:

$$\pi F_\nu = \int I_\nu \cos\theta d\omega, \tag{4.2}$$

where θ is the angle (Fig 4.1) formed by the energy flow inclined to its outward normal confined to an element of solid angle $d\omega$.

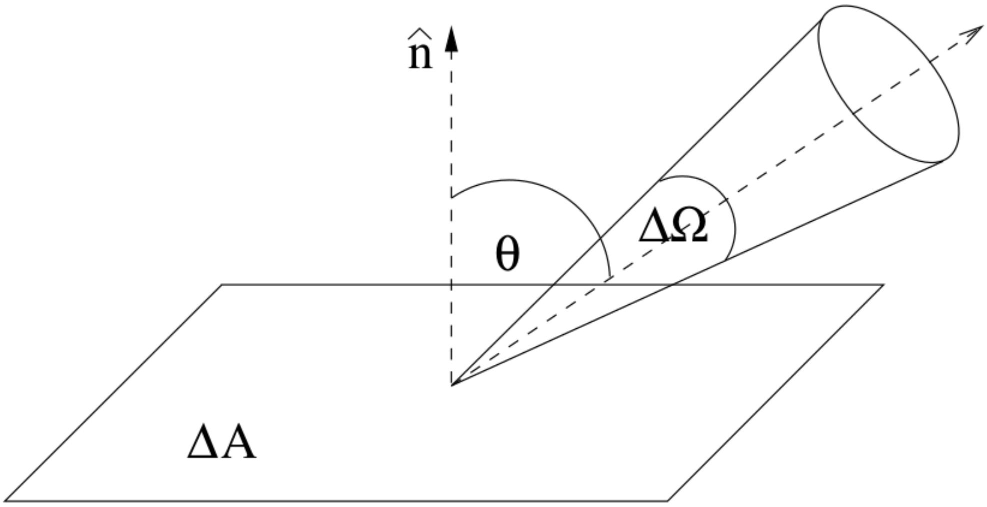

Figure 4.1: Beam of radiation

If the medium is spherical symmetric, Eq 4.1 can be re-written as

$$\mu\frac{\partial I(\nu,\mu,r)}{\partial r}+\frac{\left(1-\mu^2\right)}{r}\frac{\partial I(\nu,\mu,r)}{\partial\mu}=\eta(\nu,\mu,r)-\chi(\nu,\mu,r)I(\nu,\mu,r), \tag{4.3}$$

where r is the radius, μ is the cosine defined as $\mu = \cos\theta$, and χ is called the extinction coefficient as the sum of true absorption and scattering coefficients, and η is the thermal emission coefficient.

4.2 Continuum polarization

The radiative transfer can be represented by four variables called Stokes vector, named after George Stokes representation (Collins, 1989). The Stokes vector components describing the polarized radiation is given by the total intensity I, the difference of the two orthogonal components of the intensity, related to the polarization degree, the ellipse orientation specifying the polarization plane, and the degree of ellipticity (Chandrasekhar, 1960; Collins, 1989; Bohren and Huffman, 1998). An elliptically polarized light can be expressed as follows (Fig 4.2)

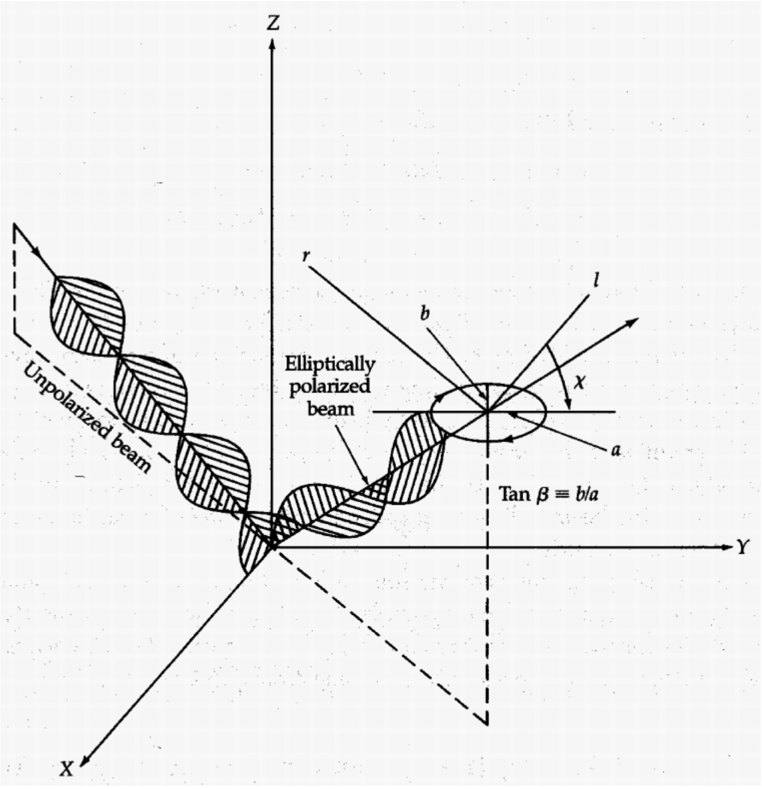

Figure 4.2: Incident unpolarized beam converted to elliptically polarized beam (Collins, 1989)

$$\begin{aligned} I =&\quad I_l + I_r = E_l^2 + E_r^2, \\ Q =&\quad I_l - I_r = E_l^2 - E_r^2, \\ U =&\quad (I_l - I_r)\tan 2\chi = 2E_l E_r \cos\epsilon, \\ V =&\quad (I_l - I_r)\tan 2\beta \sec 2\chi = 2E_l E_r \sin\epsilon, \end{aligned} \tag{4.4}$$

where tanβ represents the ratio of semi-minor to semi-major axis of the ellipse, and E_r and E_l are the amplitudes of the two orthogonal waves shifted by the phase ϵ. The subscripts r and l determine the direction of the beam if it is left or right elliptically polarized depending on the sign of β if it is positive or negative, where $0 \leq |\beta| \leq \pi/2$. The light is unpolarized, if $Q = U = V = 0$, whereas, for $V = 0$ the radiation beam is called linearly polarized with the polarization plane, making an angle χ with the l-axis.

For completely polarized beams of radiation, there exists a relationship between the Stokes parameters. The relationship is given by the equation

$$I^2 = Q^2 + U^2 + V^2, \tag{4.5}$$

furthermore, the angle between the plane of polarization and the ellipticity can be deduced from the Eq 4.4 as follows,

$$\tan 2\chi = \frac{U}{Q}, \text{ and} \tag{4.6}$$

$$\sin 2\beta = \frac{V}{\sqrt{Q^2 + U^2 + V^2}}. \tag{4.7}$$

The Stokes parameters represent the combination of the squares of amplitudes of an arbitrary light, we can easily introduce the unpolarized beam to the completely polarized beam, for this we have $I_l = I_r$ in all coordinate systems and $Q = U = V = 0$, so we the inequality relation

$$I^2 \geq Q^2 + U^2 + V^2, \tag{4.8}$$

the proof of this inequality can be found in Chapter I of the book of Chandrasekhar (1960), the ellipticity is required for the equality to occur, however for

$$I^2 > \sqrt{Q^2 + U^2 + V^2}, \tag{4.9}$$

it is necessary to introduce the natural (unpolarized) light. The Stokes parameters I and V are invariant to the rotation of the coordinate about the axis of propagation, but not the case for Q and U Collins (1989). From Eq 4.8 we can define the total polarization degree as

$$P_T = \frac{\sqrt{Q^2 + U^2 + V^2}}{I}, \tag{4.10}$$

the degree of linear polarization as

$$P_l = \frac{\sqrt{Q^2 + U^2}}{I}, \tag{4.11}$$

and the circular polarization

$$P_c = \frac{V}{I}. \tag{4.12}$$

If we rotate counterclockwise the $l - r$ coordinate frame through an angle ϕ (Fig 4.2),

$$\begin{array}{lll} Q' = & Q\cos 2\phi - U\sin 2\phi & = I\cos 2\beta\cos 2(\chi + \phi) \\ U' = & Q\sin 2\phi + U\cos 2\phi & = I\cos 2\beta\sin 2(\chi + \phi) \end{array}, \tag{4.13}$$

we can easily write in matrix-vector notation the rotation form of the Stokes parameters, because I and V are invariant to transformation of rotation.

When a photon with a specific Stokes vector, denoted as S', propagates in a certain direction (θ', φ'), and then scatters to a different direction (θ, φ), its Stokes parameters change. The new set of Stokes parameters is then given by

$$S \propto R(\Theta).L(\phi).S', \tag{4.14}$$

here $L(\phi)$ is the rotation matrix that rotates the Stokes vector into different frames, we note that Chandrasekhar used angle ψ instead of ϕ. Massive stars have winds with ionized gas, as a result we expect a rise in polarization due to electron scattering (called Thomson scattering). The scattering matrix $R(\Theta)$ for electrons, where Θ is the angle of scattering measured from the direction of the incident photon, is given by (Chandrasekhar, 1960; Code and Whitney, 1995)

$$R(\Theta) = \frac{3}{4}\begin{pmatrix} \cos^2\Theta + 1 & \cos^2\Theta - 1 & 0 & 0 \\ \cos^2\Theta - 1 & \cos^2\Theta + 1 & 0 & 0 \\ 0 & 0 & 2\cos^2\Theta & 0 \\ 0 & 0 & 0 & 2\cos^2\Theta \end{pmatrix}. \tag{4.15}$$

Continuum polarization in massive stars is primarily caused by the interaction between incident radiation and free electrons in the stellar atmosphere. This interaction, known as electron scattering, leads to the polarization of the emitted light. The degree and direction of polarization can provide valuable information about the physical properties of these stars.

Studies conducted by Hillier and Miller (1998) and Vink et al. (2002) have shown that the continuum polarization is sensitive to various factors. These include the density and velocity structure of the stellar wind, as well as the orientation of the scattering region relative to the observer. By analyzing the continuum polarization, researchers can gain insights into crucial parameters like the mass-loss rates and wind geometries of massive stars. Furthermore, line polarization observations have played a crucial role in investigating the presence of magnetic fields in these stars. The work of Donati et al. (2002) highlights how the analysis of line polarization can provide valuable information about the existence and characteristics of magnetic fields in massive stars.

Overall, the study of line polarization due to electron scattering has become an essential tool for understanding the complex atmospheres and winds of massive stars. It contributes to our knowledge of stellar evolution and aids in the exploration of magnetic fields in these objects.

Chapter 5

Numerical methods

Many physical problems are described by partial differential equations (PDEs), including Maxwell's equations of electromagnetism, some fundamental laws of nature like fluid dynamics, or general relativity (Springel, 2016). For PDEs we can not get a general solution for these types of equations, a call for numerical method is needed to tackle the difficulties. Several methods are commonly used in astrophysics, like finite difference method, finite volume method, and Monte Carlo method. In this chapter we will show an overview of the methods used during our studies, we will mainly focus on numerical hydrodynamics and some brief discussion about Monte Carlo method.

5.1 Eulerian hydrodynamics

The mathematical description of Euler hydrodynamic equations, is based on the combination of continuity, momentum, and energy equations. Eulerian methods can be divided into two groups: finite difference, and finite volume methods.

5.1.1 Simple advection

First-order hyperbolic equations are useful to introduce the numerical method, they also used to address a non-linear conservation laws (LeVeque et al., 2002; Springel, 2016). We start by the simple advection equation in one dimension

$$\frac{\partial u}{\partial t} + v.\frac{\partial u}{\partial x} = 0, \tag{5.1}$$

where $u = u(x,t)$ is a function of x and t, and v is a constant parameter. Let $q(x)$ a function space dependent, then

$$u(x,t) = q(x - vt) \tag{5.2}$$

We can easily check that $q(x)$ is a solution of the PDE, we can see $u(x,t=0) = q(x)$ as an initial condition and then this is copied at a later time simply by translation vt along the $x-$direction (Fig 5.1(Springel, 2016)).

Let's try to solve the advection equation numerically, for example using the method of line, eq-5.1 becomes

$$\frac{du_i}{dt} + v\frac{u_{i+1} - u_{i-1}}{2h} = 0, \tag{5.3}$$

where i is the grid index, and h is the spacing. Further, we can discretize the time derivative with a forward scheme we can get

$$u_i^{n+1} = u_i^n - v\Delta t \frac{u_{i+1}^n - u_{i-1}^n}{2h}, \tag{5.4}$$

here Δt is the time step, and n is the time grid.

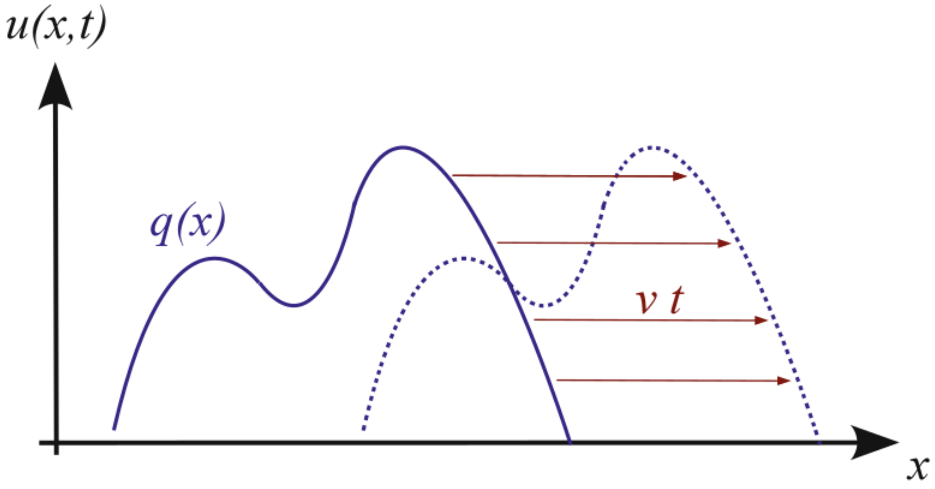

Figure 5.1: Advection with constant velocity (Springel, 2016).

To compute this formula we need initial and boundary conditions in order to update the solution in the grid. Applying for example a step function, one obtains strong oscillatory errors in downstream region of the step, which render the numerical solution unstable and lead to the failure of the method. In order to obtain an acceptable approximation we need to impose some conditions. These conditions are defined as *accuracy*, *stability* and *convergence*. These 3 conditions cover different aspects to the relation between the numerical solution and the analytical solution of the differential equation.

To update the u_i, the information is derived from upstream (u_{i-1}) and downstream (u_{i+1}). The information should flow in the direction of the stream and as a result u_i should not really depend on the downstream side at all. So lets change the space derivative to backward difference (*upwind scheme*)

$$\frac{du_i}{dt} + v\frac{u_i - u_{i-1}}{h} = 0. \tag{5.5}$$

The discretization now depends on the sign of v. For negative v one has to use forward difference instead

$$\frac{du_i}{dt} + v\frac{u_{i+1} - u_i}{h} = 0. \tag{5.6}$$

Lets rewrite the upwind schemes of the spatial derivative as

$$\frac{u_i - u_{i-1}}{h} = \frac{u_{i+1} - u_{i-1}}{2h} - \frac{u_{i+1} - 2u_i + u_{i-1}}{2h}. \tag{5.7}$$

Hence the stable upwind schemes can be written as

$$\frac{du_i}{dt} + v\frac{u_{i+1} - u_{i-1}}{h} = \frac{vh}{2}\frac{u_{i+1} - 2u_i + u_{i-1}}{h^2}. \tag{5.8}$$

Recall that

$$\frac{\partial^2 u}{\partial x^2} = \frac{u_{i+1} - 2u_i + u_{i-1}}{h^2}, \tag{5.9}$$

which is the Laplacian (diffusion) expressed as finite difference; if we define $D = \frac{vh}{2}$, we are solving the following equation

$$\frac{\partial u}{\partial t} + v.\frac{\partial u}{\partial x} = D\frac{\partial^2 u}{\partial x^2} \tag{5.10}$$

and not the original advection equation. The diffusion term on the right hand side is here as a result of numerical algorithm that we have used, which is needed to be added to obtain the stability of the integration. We can see that for better grid resolution $h \to 0$ the diffusion term becomes smaller and we can obtain better solution. To get larger diffusivity we need larger velocity v so faster advection the stronger the numerical diffusion effects become.

5.1.2 Riemann problem

The Riemann problem consists of an initial value problem for hyperbolic equations, together with two piece-wise constant states that meet a plane where $t = 0$ (Springel, 2016).

5.1.3 Finite volume method

The most common method user to solve hydrodynamic equations in astrophysics is the finite volume method, or in other hand the *Riemann* solvers, the hyperbolic conservation laws (LeVeque et al., 2002; Springel, 2016) can be written as

$$\frac{\partial U}{\partial t} + \nabla.\boldsymbol{F} = 0 \tag{5.11}$$

where $\boldsymbol{U}$ is the state vector and $\boldsymbol{F}$ is the flux vector, and ∇ is the gradient. The Euler model equation (Eq 2.1-2.3) can be written in the form

$$\boldsymbol{U} = \begin{pmatrix} \rho \\ \rho\boldsymbol{v} \\ \rho e \end{pmatrix}, \tag{5.12}$$

$$\boldsymbol{F} = \begin{pmatrix} \rho\boldsymbol{v} \\ \rho\boldsymbol{v}\boldsymbol{v}^T \\ (\rho e + P)\boldsymbol{v} \end{pmatrix} \tag{5.13}$$

here e represents the specific energy, $e = U_\mathrm{T} + \boldsymbol{v}^2/2$ and U_T is the thermal energy per unit mass. To close the system we recall the ideal gas law, which gives the pressure

$P = (\gamma - 1)\rho U_{\mathrm{T}}$. The finite volume schemes consists of averaging the state over a set of finite cells, these cell averaged as

$$\boldsymbol{U}_i = \frac{1}{V_i}\int_{cell\quad i} \boldsymbol{U}(\boldsymbol{x})dV. \tag{5.14}$$

We can now update the cell-averaged quantities, by integrating the conservation law over finite interval in time and over a cell

$$\int_{x_{i-1/2}}^{x_{i+1/2}} dx \int_{t_n}^{t_{n+1}} dt\left(\frac{\partial \boldsymbol{U}}{\partial t} + \frac{\partial \boldsymbol{F}}{\partial x}\right) = 0, \tag{5.15}$$

which gives

$$\int_{x_{i-1/2}}^{x_{i+1/2}} dx\,[\boldsymbol{U}(x,t_{n+1}) - \boldsymbol{U}(x,t_n)] + \int_{t_n}^{t_{n+1}} dt\,[\boldsymbol{F}(x_{i+1/2},t) - \boldsymbol{F}(x_{i-1/2},t)] = 0. \tag{5.16}$$

We see that the first term is the cell average (similar to Eq 5.14), and then the integral becomes

$$\Delta x\,[\boldsymbol{U}(x,t_{n+1}) - \boldsymbol{U}(x,t_n)] + \int_{t_n}^{t_{n+1}} dt\,[\boldsymbol{F}(x_{i+1/2},t) - \boldsymbol{F}(x_{i-1/2},t)] = 0. \tag{5.17}$$

Now, for each time step $t > t_n$, the function $\boldsymbol{F}(x_{i+1},t)$ can be determined by solving the Riemann problem. At the interface, the solution depends on the left state $\boldsymbol{U}_i^n$ and the right state $\boldsymbol{U}_{i+1}^n$ of the current time. Therefore, we can express this as follows:

$$\boldsymbol{F}(x_{i+1/2},t) = \boldsymbol{F}^{\star}{}_{i+1/2}, \tag{5.18}$$

where $\boldsymbol{F}^{\star}{}_{i+1/2} = \boldsymbol{F}_{\mathrm{Riemann}}\left(\boldsymbol{U}_i^n, \boldsymbol{U}_{i+1}^n\right)$ is a short notation for the corresponding Riemann solution. Replacing in Eq 5.17, we get

$$\Delta x\left[\boldsymbol{U}_i^{n+1} - \boldsymbol{U}_i^n\right] + \Delta t\left[\boldsymbol{F}^{\star}{}_{i-\frac{1}{2}} - \boldsymbol{F}^{\star}{}_{i+\frac{1}{2}}\right] = 0, \tag{5.19}$$

in explicit form can be written as:

$$\boldsymbol{U}_i^{n+1} = \boldsymbol{U}_i^n + \frac{\Delta t}{\Delta x}\left[\boldsymbol{F}^{\star}{}_{i-1/2} - \boldsymbol{F}^{\star}{}_{i+1/2}\right], \tag{5.20}$$

where the term in the bracket gives the flux flowing from the left of the cell and the flux flowing out of the cell on its right. Godunov came up with the idea of using the Riemann solution in the updating step, which is why such schemes are sometimes referred to as Godunov schemes (Springel, 2016).

5.2 Godunov's method

Godunov's original methodology employs the most basic reconstruction scheme, which relies on piecewise constant segments. This approach intuitively leads to Riemann problems at cell interfaces (LeVeque et al., 2002; Castor, 2007). We can consider the flow variables to be zone averages, and we can find their evolution by finding the gains and losses of conserved quantity at each zone. This is called Reconstruct-Evolve-Average schemes (REA) (Springel, 2016). An update scheme of a hydrodynamical system discretized on a mesh, using the REA, can be seen as a series of three successive steps (Springel, 2016): *i)* the cell-averaged quantities (Fig 5.2) can be used to determine the variation of these quantities throughout the cell. The sketch assumes a piece-wise constant reconstruction method, which is the most basic approach with a first-order level of accuracy.

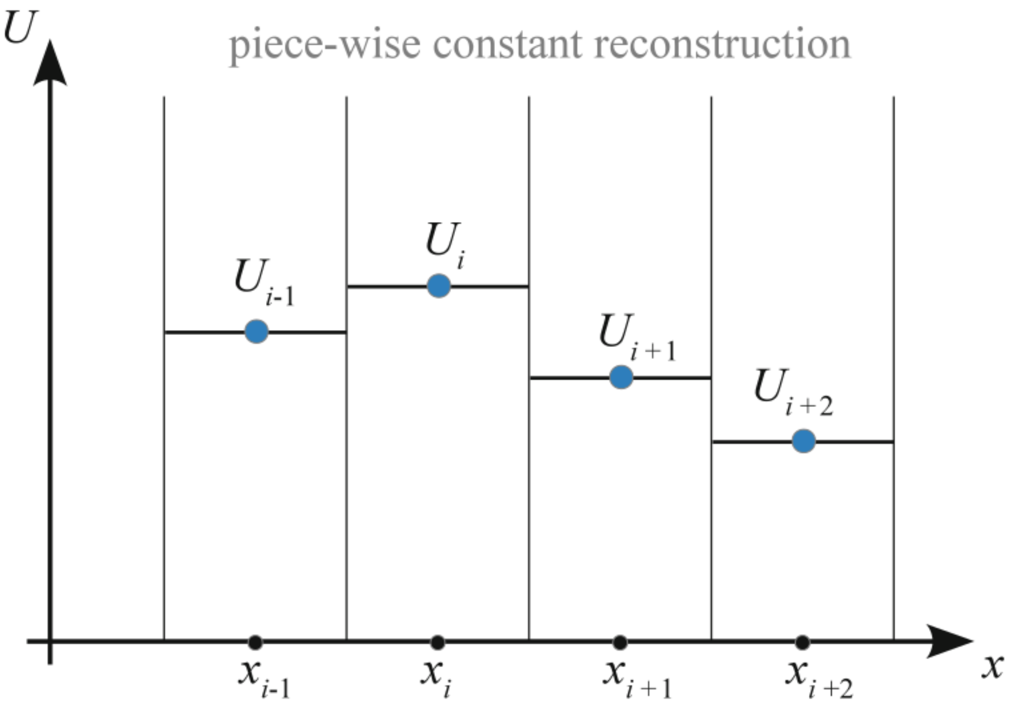

Figure 5.2: Piecewise constant states of a fluid that represent the simplest possible reconstruction of its state based on a set of discrete values U_i is known at spatial coordinates x_i (Springel, 2016).

ii) The reconstructed state is then advanced in time by Δt using the Godunov's approach, which treats each cell interface as a piece-wise constant initial value problem that is solved either exactly or approximately with the Riemann solver. This method is mathematically valid as long as the waves originating from opposite sides of a cell do not begin to interact. However, in practice, it is necessary to set a maximum time step Δt to prevent this interaction from occurring. *iii)* The wave structure that arises from the progression over a time step Δt is averaged in a conservative manner to calculate new states U^{n+1} for each cell. There is no need to explicitly perform the averaging step; instead, it can be accomplished by accounting for the fluxes that enter or exit the control volume of the cell. This process is then repeated in its entirety.

5.2.1 WENO

The subsequent category of Eulerian hydrodynamics schemes is known as the Essentially Non-Oscillatory class (ENO) and its derivative, the Weighted Essentially Non-Oscillatory (WENO) class (Castor, 2007). In order to comprehend these schemes, it is important to first discuss the Lax-Wendroff (Lax and Wendroff, 1960) method. This method is used for solving a system of conservation laws in one dimension, such as the Euler equations. The Lax-Wendroff method involves a two-step process: prediction and correction.

$$\boldsymbol{U}^{n+1/2}_{i+1/2} = \frac{1}{2}\left(\boldsymbol{U}^{n}_{i+1} + \boldsymbol{U}^{n}_{i}\right) - \frac{\Delta t}{2\Delta x}\left[\boldsymbol{F}^{n}_{i+1} - \boldsymbol{F}^{n}_{i}\right], \tag{5.21}$$

$$\boldsymbol{U}^{n+1}_{i} = \boldsymbol{U}^{n}_{i} - \frac{\Delta t}{2\Delta x}\left[\boldsymbol{F}^{n+1/2}_{i+1/2} - \boldsymbol{F}^{n+1/2}_{i-1/2}\right]. \tag{5.22}$$

It can be observed that the predictor equation calculates a solution vector at the half-time-step point by utilizing the fluxes evaluated at zone centers based on the initial step values. The corrector step then applies the edge-centered fluxes, derived from the half-time-step unknowns, to update the zone-centered unknowns in a conservative manner.

5.2.2 Adaptive mesh refinement

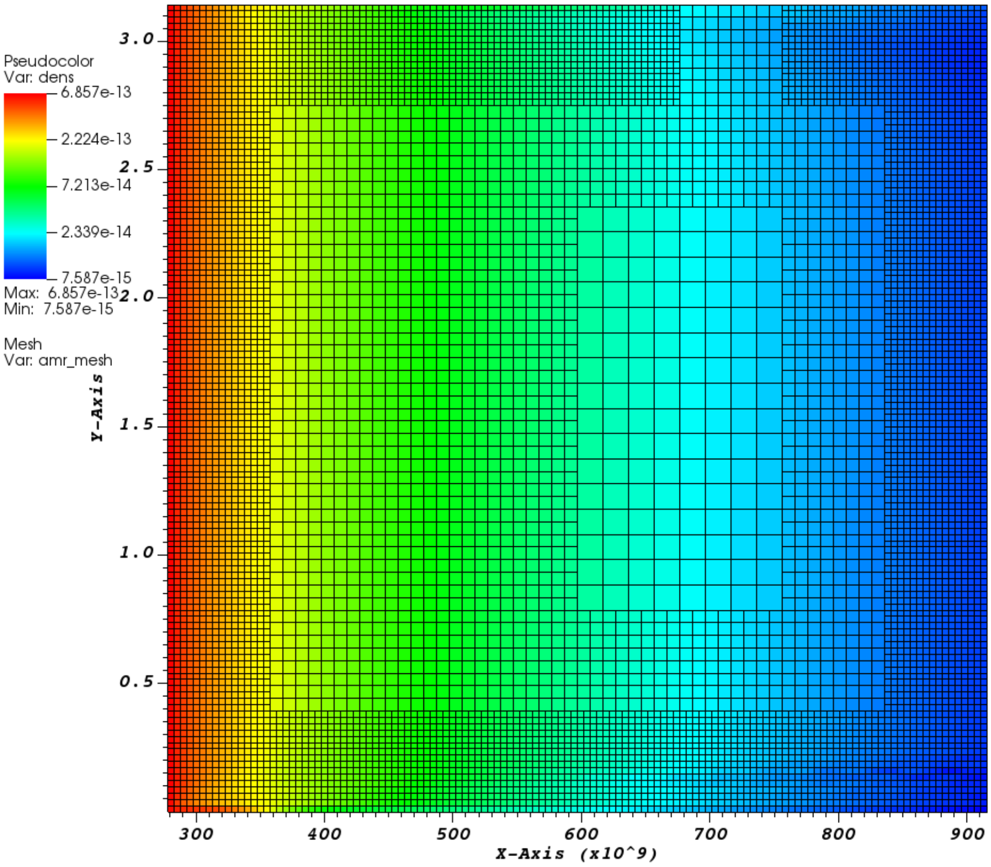

Figure 5.3: Wind density model in cgs units computed using AMR.

The concept of Adaptive Mesh Refinement (AMR) aims to provide higher grid resolution in the parts of the spatial domain that require it the most at any given time. While it might be possible to implement AMR in a Lagrangian framework, the need for this capability is reduced as the Lagrangian zones automatically adjust to follow the material and tend to be where additional resolution is required (Castor, 2007). However, there may still be situations where extra resolution near shocks, for example, is necessary as they move through the material. The second reason for not using Lagrangian AMR is that it could become complex and burdensome. An example of an AMR solution is shown in Fig 5.3. The test problem was computed using the FLASH code (Fryxell et al., 2000) for the stellar wind model, where we implemented the CAK line force into the code (section 6.3).

5.3 Monte Carlo method of the radiative transfer

The Monte Carlo method, a powerful computational technique, has been extensively utilized in astrophysics to solve the radiative transfer equation. This method employs random sampling to approximate complex physical processes and systems, making it particularly well-suited for addressing the challenges posed by the radiative transfer equation (see, for example, Harries 2000).

In astrophysics, the radiative transfer equation is vital for understanding the propagation of radiation through various media, such as stellar atmospheres and interstellar clouds. The Monte Carlo method simplifies this task by simulating the random paths of individual photons as they interact with the surrounding medium. By tracking a sufficient number of photons, the method can provide valuable insights into the overall behavior of radiation in these environments (Whitney, 2011).

One of the key advantages of using the Monte Carlo method in astrophysics is its flexibility; it can readily accommodate complex geometries and a wide range of scattering, absorption, and emission processes. This has led to its widespread adoption in various astrophysical applications, including modeling the radiation fields in star-forming regions, simulating the propagation of light in accretion disks, and studying the radiative properties of dust grains (Bianchi and Ferrara, 2005).

5.3.1 Simple scattering

The Monte Carlo method for radiative transfer (MCRT) is an approach that uses probabilistic methods to simulate the transport of individual 'photon packets' (or photons). This method involves describing all radiation sources, tracing a path for each photon that includes all interactions, and tabulating relevant parameters such as intensity, flux, angle of exit, position of exit (for imaging), and wavelength (Whitney, 2011). This process is essentially a random walk for each photon, and the resulting data can provide valuable insights into how radiation interacts with different materials and media.

5.3.2 Sampling technique

Monte Carlo simulation is based on random sampling of probability distribution function (PDF) in association with the physical processes that are being simulated. The continuous probability distribution function $f_X(x)$ is analogue to the discrete probability distribution of a random variable X with the value x(Noebauer and Sim, 2019). The cumulative probability distribution $F_X(x)$ given as

$$F_X(x) = \int_{-\infty}^{x} f_X(x')dx' \tag{5.23}$$

is a monotonic function with values between zero and one. The simplest method for random sampling consists of matching the cumulative distribution functions of both the reference distribution and the distribution in question. In particular, by using a random number z and ensuring that the associated cumulative probability functions are equal ($F_X(x) = F_Z(z)$), a discrete value x that represents the probability distribution $f_X(x)$ can be determined. As a result, this technique for taking random sampling needs an analysis of the cumulative distribution function $F(x)$ to be done in reverse. For instance, when the radiation field is isotropic ($f_\mu(\mu) = \frac{1}{2}$), the direction of propagation is determined by resolving

$$\int_{-1}^{\mu} d\mu' \frac{1}{2} = \int_{0}^{1} dz'.1 \tag{5.24}$$

giving $\mu = 2z - 1$. However, there may be complex distributions for which the corresponding cumulative distribution functions cannot be easily inverted. An example of this is the drawing of the initial packet frequencies in accordance with a thermal radiation field, governed by the Planck distribution. In such cases, the rejection method may be used to perform the random sampling process. In its simplest version, which is often referred to as von Neumann rejection sampling (Neumann, 1951), pairs of random numbers are drawn (z_x, z_y), which are then mapped onto the support and image of the probability distribution.

5.3.3 Random number

The sampling and MCRT calculation in the above outline requires some form of randomness, which is difficult to achieve on a deterministic computer. However, a (pseudo) Random Number Generator (RNG) can provide " pseudo-randomness" that is sufficient for many purposes. These algorithms produce sequences of numbers ξ, which are typically uniformly distributed over the interval [0, 1] based on a starting value (seed). Although they are generated by deterministic prescriptions, such sequences share statistical properties with true randomness (Noebauer and Sim, 2019). A well-known example of such algorithms is the family of linear congregational methods. A new random number ξ_{i+1} is generated based on a previous draw, and a set of large numbers, a, c, and M, the new generated random number is given by

$$\xi_{i+1} = (a\xi_i + c) \mod M. \tag{5.25}$$

5.3.4 Computing flux and intensity

In order to determine the specific intensity of the photons that exit the binning process, we will refer to a study conducted by Chandrasekhar (1960)

$$I_\nu = \frac{dE_\nu}{\cos\theta d\nu dA dt d\omega}, \tag{5.26}$$

where dE_ν is the energy at frequency interval $(\nu,\ \nu+d\nu)$, and θ is the angle of exit to the normal of a surface with area dA into a solid angle $d\omega$ over time dt. This represents a narrow beam of radiation emitted from the surface of the atmosphere. Assuming we are considering monochromatic photons with no time dependence, let's denote the number of photons exiting at specific angles μ_i and φ_j as $N_{i,j}$. In this case, the intensity of the radiation, denoted as $I_{i,j}$, can be calculated using the given formula (Whitney, 2011)

$$I_{i,j} = \frac{h\nu N_{i,j}}{\mu_i \Delta\mu \Delta\phi dA dt}. \tag{5.27}$$

The observed intensity of light is often measured and expressed in terms of flux F. According to Chandrasekhar (1960), the rate at which energy flows across a surface per unit area per unit frequency interval can be calculated by integrating the intensity $I(\mu,\varphi)$ over all angles. This can be represented by (Whitney, 2011)

$$\pi F = \int_{-1}^{1}\int_{0}^{2\pi} I(\mu,\varphi)\mu d\mu d\phi. \tag{5.28}$$

To put it into perspective, let's assume N_0 photons are incident at a cosine angle μ_0. In that case, the net rate of energy flow can be calculated as

$$\pi F = \frac{h\nu N_0}{\mu_0 dA}, \tag{5.29}$$

where ν denotes the frequency of the photons. By rearranging the equation, we can express the intensity $I_{i,j}$ in terms of the flux F as

$$\frac{I_{i,j}}{F} = \frac{\pi\mu_0 N_{i,j}}{\mu_i N_0 \Delta\mu\Delta\phi}. \tag{5.30}$$

Here, $N_{i,j}$ represents the number of photons incident at a specific angle μ_i and azimuthal angle φ_j, while $\Delta\mu$ and $\Delta\varphi$ are the small intervals over which the integration is performed.

5.4 Scattering and polarization

Astrophysical applications typically focus on scattering problems such as electron scattering, Compton scattering, resonance line scattering, and dust scattering. In many cases, the angular dependence of the scattering phase function, known as the scattering function, can be approximated analytically or computed numerically and represented in tabular form. The Monte Carlo method is a commonly used technique to solve these scattering problems, including polarization components (Whitney, 2011). In Figure 5.4, a diagram illustrates the scattering process of a photon from the direction P_1 to direction P_2. Analytically describing the phase function for scattering problems is straightforward for angles relative to P_1, but for polarization problems, the frame of reference must be considered, necessitating the use of Müller matrices and rotation into and out of the photon propagation direction (Chandrasekhar, 1960; Code and Whitney, 1995; Whitney, 2011). We consider here the linear polarization as described in Chap 4, we use the Stokes vector for the polarization

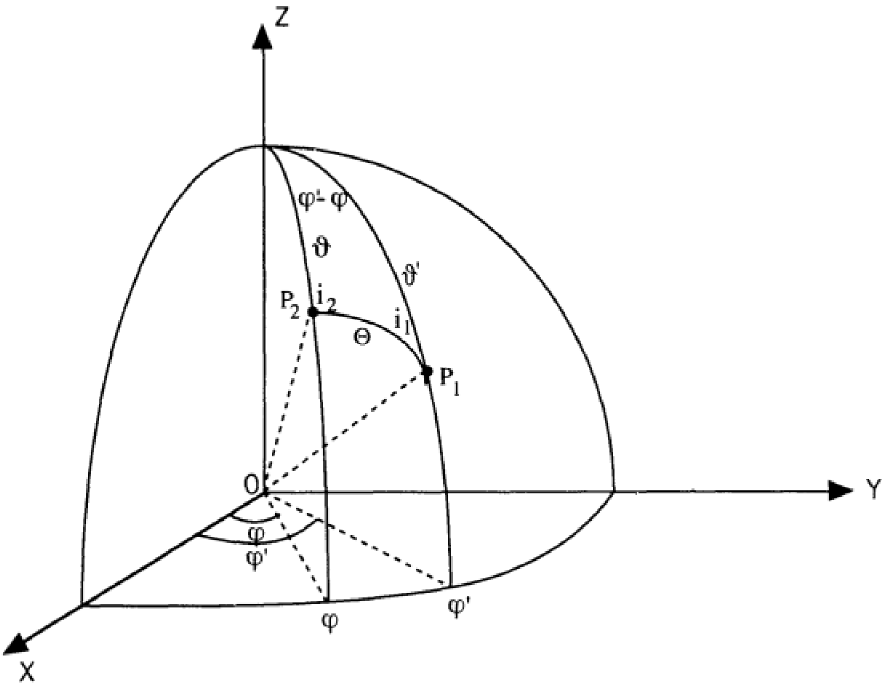

Figure 5.4: Geometry for scattering. A photon propagating into direction $P_1(\theta',\varphi')$ in the observer's frame) scatters through the angle Θ into direction $P_2(\theta,\varphi)$ (Code and Whitney, 1995)

$$S = [I(\Theta,\phi), Q(\Theta,\phi), U(\Theta,\phi), V(\Theta,\phi)]\,. \tag{5.31}$$

For electron scattering, the elements of the rotation matrix (see Chap 4) are

$$\begin{array}{lcll} P_{11} & = & P_{22} = \cos^2\Theta + 1 & = \mu^2 + 1 \\ P_{12} & = & P_{21} = \cos^2\Theta - 1 & = \mu^2 - 1 \ , \\ P_{33} & = & P_{44} = 2\cos\Theta & = 2\mu \end{array} \tag{5.32}$$

where $\mu = \cos\Theta$, and the rest of the other elements are zeros. In this case, we compute the Stokes I parameter in the reference frame of the photon using

$$S = L(\pi - i_2) R(\Theta) L(-i_1) S', \tag{5.33}$$

this gives

$$I = \left(\mu^2 + 1\right) I' + \left(\mu^2 - 1\right) \cos^2 i_1 Q' - 2\mu \sin^2 i_1 U'. \tag{5.34}$$

Ultimately, the goal is to sample the scattering direction (μ, i_1) based on the computed function. We could sample i_1 (Fig 5.4) and μ from a uniform distribution so that (Code and Whitney, 1995)

$$i_1 = 2\pi\xi_1, \tag{5.35}$$

$$\mu = 1 - 2\xi_2, \tag{5.36}$$

where ξ_1 and ξ_2 are two random numbers generated by the computer. The next step involves calculating the new Stokes parameter using Eq 5.33. However, for greater accuracy, it is recommended to sample from a probability distribution function that is a closer approximation to the exact distribution. In the case of Thomson scattering, sampling from the exact probability distribution can be achieved using the rejection method. The process is as follows: First, we choose values for μ and i_1 from a uniform distribution and use them to calculate the I Stokes parameter. Then, a random number y is selected within the range of minimum and maximum values of the probability distribution for all angles and Stokes parameters (Code and Whitney, 1995; Whitney, 2011),

$$y = \xi_3 \left(I_{\max} - I_{\min} \right). \tag{5.37}$$

To ensure that angles are sampled according to their probability, we reject angles where y is greater than I and select again until I becomes greater than y. This method guarantees that the angle distribution is sampled with the appropriate frequency. The efficiency of this method can be measured by comparing the area of the probability distribution to the smallest box that can encompass it, or by comparing the number of accepted angles to the total number of attempts. In the case of Thomson scattering, the efficiency is 66%, which is considered reasonably high (Code and Whitney, 1995).

The code presented below provides a high-level overview of the technique, but for a more comprehensive understanding, please refer to the work of Code and Whitney (1995) and Wood et al. (1996). The technique employed in this code follows a Monte Carlo approach and can be summarized in the following steps:

1. A photon packet, which is not polarized, is emitted randomly from a random location on the surface of a spherical star.

2. To determine the distance the photon will travel before scattering, a random optical depth, denoted as τ, is generated using the equation $\tau = -\log \xi$.

3. Follow the path of the photon and integrate it until it reaches the optical depth, $\tau = \int n_e \sigma_T ds$, where n_e represents the electron number density and σ_T is the Thomson scattering cross section.

4. Use the scattering phase function, also known as the differential cross section, to generate a new random direction for the photon. This involves generating a random scattering angle and calculating the new Stokes parameters of the scattered photon.

5. Repeat steps 2 to 4 until the photon exits the envelope. If the photon intersects with the star, remove it and emit a new photon (go back to step 1). This accounts for the occultation of the scattered light by the star.

6. Tally relevant quantities of interest by grouping the flux and polarization based on the directions of observation.

7. Emit a new photon from the star (go back to step 1).

8. Repeat steps 1 to 7 until the emergent flux and polarization results have sampling errors that are sufficiently small.

Polarization in massive stars has been extensively studied using the Monte Carlo method as a powerful numerical technique that allows for the realistic modeling of complex physical processes. In particular, researchers have employed Monte Carlo simulations to investigate the impact of electron scattering on the polarization properties of these stellar objects.

By considering various factors such as the scattering phase function and the Thomson cross section, Monte Carlo simulations can accurately capture the intricate interaction between photons and electrons in massive stars. A noteworthy contribution to this field is the work of Code and Whitney (1995), which provided a comprehensive framework for simulating the scattering process in these stars.

Through these simulations, it becomes possible to calculate the polarization properties of massive stars and gain insights into their internal structure and magnetic fields. The analysis of polarization in these objects offers valuable information about their formation, evolution, and circumstellar environments (Halonen and Jones, 2013). Furthermore, researchers have also explored the effects of multiple scattering on polarization by utilizing Monte Carlo radiative transfer codes. This has allowed them to investigate polarization in stellar wind bow-shock nebulae (Shrestha et al., 2018).

Chapter 6

Modeling of stellar winds of rotating, hot and massive stars

Hydrodynamic modeling of stellar winds including a wind-compressed disk in massive stars is a complex and challenging problem in astrophysics. Such models are essential to understanding the mass-loss processes and evolution of massive stars, which play a crucial role in the chemical enrichment and energy balance of the universe. These winds are composed of highly ionized gases that are accelerated to high velocities due to the intense radiation from the star's surface. Understanding the properties of these winds is important for many astrophysical phenomena such as the evolution of galaxies, the formation of stars and planets, and the distribution of chemical elements in the universe. Numerical models are used to simulate the complex processes that occur in the stellar winds of hot stars. These models incorporate the principles of gas dynamics, radiation transfer, and the effects of magnetic fields to predict the velocity, temperature, and density of the wind as it flows outwards from the star. These models also take into account the properties of the star itself such as its mass, luminosity, and surface temperature.

6.1 Wind compressed disk

To explain the presence of disk observed around Be stars, Bjorkman and Cassinelli (1993, BC hereinafter) developed a semi-analytical model that shows that the disk is generated due to two factors: Firstly, the wind at the equator of the star is deflected, and secondly, the streamlines crossing the equatorial plane lead to the formation of the disk. Be stars are a type of B-class the star that displays prominent emission lines in their spectra, indicating the presence of a circumstellar disk composed of gas and dust. The disks around Be stars are thought to form as a result of the star's rapid rotation, which generates a centrifugal force that can counteract the gravitational force of the star, allowing material to accumulate in a disk. Hydrodynamic modeling by Owocki, Cranmer, and Blondin (1994) showed that the approximations used by BC are valid with minor modifications. Since our work mainly consists of numerical modeling, we set up the hydrodynamic code that incorporates the relevant stellar parameters.

We employed the VH-1 code developed by Blondin et al. (1990) modified by Owocki, Cranmer, and Blondin (1994), which uses the piecewise parabolic method (PPM) algorithm, and coupled it with the subroutine created by Owocki, Cranmer, and Gayley (1996) to determine the radiative force and solve the hydrodynamic model equations. The PPM algorithm, a third-order finite difference scheme developed by Colella and Woodward (1984), was employed. The VH-1 code allows for the solution of hydrodynamic equations in various geometries, including 1D, 2D, and 3D planar, cylindrical, and spherical. To incorporate the oblate stellar surface due to rotation, the lower boundary condition in the radial direction is crucial in the hydrodynamic simulation of stellar winds. To address this issue, we adopted the specified stair-casing boundary condition proposed by Owocki, Cranmer, and Blondin (1994). Additionally, we set the base wind density to a constant value proportional to the mass loss rate $\dot{M}$ to ensure a subsonic inflow of matter at the base of the wind where

$$\rho(r = R_\star) \propto \frac{\dot{M}}{4\pi R_\star^2 c_s}. \tag{6.1}$$

We made different assumptions for the radial and azimuthal velocity components. Specifically, we considered a subsonic outflow for the radial velocity and rigid body rotation for the azimuthal velocity. For latitudinal velocity, we used the same subsonic outflow as the radial velocity. To account for the oblateness of the stellar surface, we defined the radius as a function of colatitude θ and the ratio of rotational velocity and the critical velocity $\bar{\omega}$ (see Eq 3.9), where the critical velocity (Eq 3.7) is given by

$$v_{\text{crit}} = \sqrt{\frac{2GM_\star}{3R_\star}}. \tag{6.2}$$

As for the upper boundary, we implemented an outflow condition. In the latitudinal direction, we applied reflecting boundary conditions due to the symmetry, which was already implemented by default in the VH-1 code.

To perform the time-dependent calculations, we need to specify an initial condition for each flow variable across the spatial mesh at the starting time $t = 0$. Our experiments show that if the outer part of the initial wind outflow is significantly supersonic, the models eventually converge to the same 2D steady flow solution. Therefore, we set the initial state by fitting a 1D mCAK wind model onto the oblate stellar surface at each latitude (Owocki, Cranmer, and Blondin, 1994).

The model is then evolved in time using fixed time steps, which are set to a fraction of the Courant time. To maintain numerical stability in the time integration process, we adopted the Courant time (CFL) of 0.2 to ensure numerical stability. Hence, this value is used in all the models presented here.

6.1.1 Be stars

Our simulation involves applying the model setup to a typical massive stars. We begin by simulating the star with spectral type B2.5, using the same grid setup and boundary conditions as in Owocki, Cranmer, and Blondin (1994). In the radial direction, we use $n_i = 296$ grid points, and in the latitudinal direction, we use $n_j = 120$ grid points. The star has a mass of $M_\star = 7.5 M_\odot$, a radius $R_\star = 4 R_\odot$, a luminosity $L_\star = 2310 L_\odot$, and an effective temperature $T_{\text{eff}} = 2.10^4 K$, we limit our model for this star to a rotation of $v_{\text{rot}} = 350$ km.s^{-1}.

The CAK line force parameters are (Owocki, Cranmer, and Blondin, 1994, Table 1) $\alpha = 0.51$, $k = 0.6$, and $\delta = 0.166$.

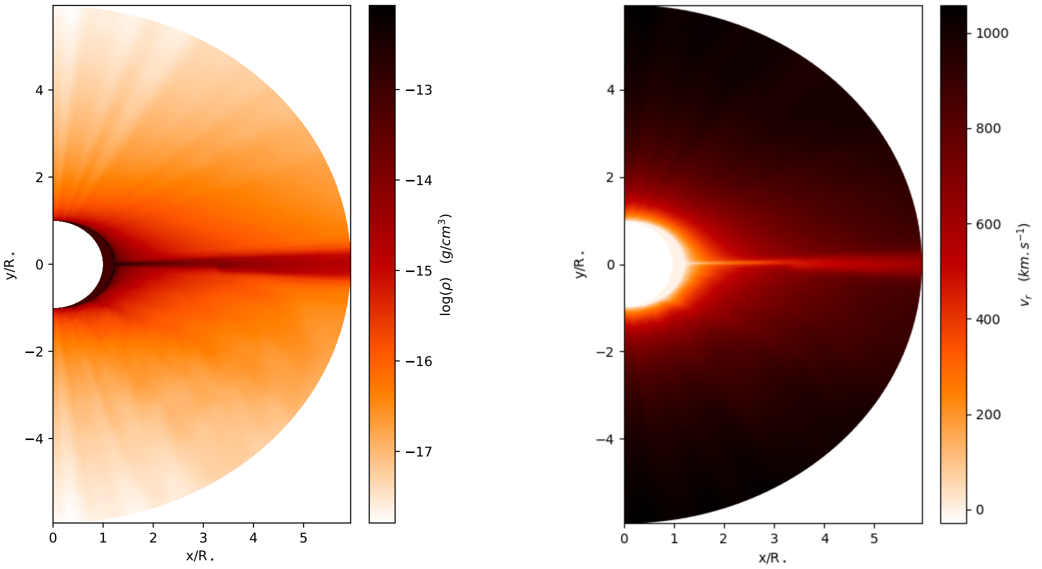

Figure 6.1: Surface plot in logarithmic scale of the density (*left*), and radial velocity (*right*) of Be star, showing the wind compressed disk model.

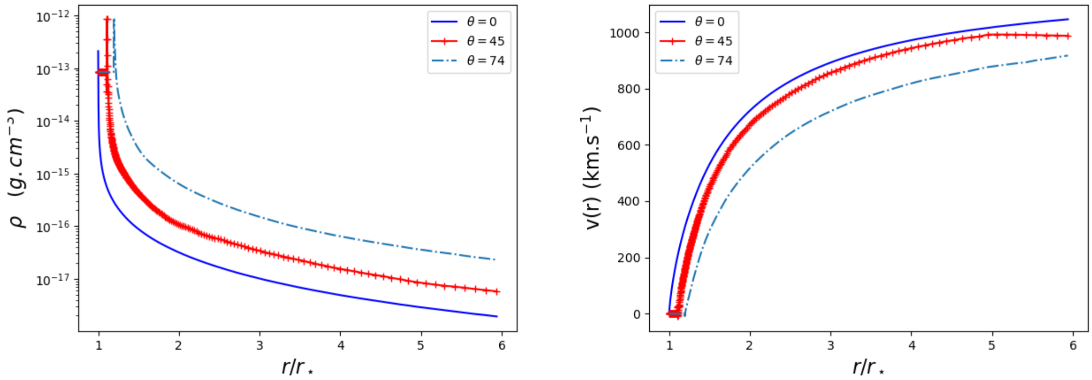

Figure 6.2: Linear plot as function of radius for the density (*left*), and radial velocity (*right*) for different angles θ for $v_{\mathrm{rot}} = 350$ km.s^{-1}, for Be star.

Figure 6.1 shows a surface plot of the density and radial velocity, we can see the flow toward the equator forms a compressed density of material moving outward from the stellar surface. This provides a good view of the flow estimate, consisting of low-density and fast flow at the polar regions and dense outflow at the equator; we note the symmetry at the equatorial plane. Figure 6.2 shows line plots for the density and velocity for various co-latitudes as a function of radius. The plots show the increase of the density from the pole toward the equator, on the other hand, the velocity decreases from the pole to the equator, while reaches its highest magnitude at the polar sides. These results confirm the prediction by BC.

6.1.2 Wolf Rayet stars

Wolf-Rayet (WR) stars are massive stars that have shed their hydrogen envelope in the course of their evolution (Conti, 1975; Chiosi, Nasi, and Bertelli, 1979; Sander, Hamann, and Todt, 2012). The collapse of WR stars that spin at a high rate can give rise to long-duration gamma-ray bursts, as hypothesized by Woosley (1993) and proposed by Vink and de Koter (2005) that these stars can be progenitors of such bursts. However, due to difficulties in accurately measuring the rotational velocities of Wolf-Rayet stars, it is challenging to test this model using direct observations. Nonetheless, we can use polarized light as an indirect means of estimating rotational velocities and evaluating the nature of gamma-ray burst progenitors. Stevance et al. (2018) applied spectropolarimetry technique to measure the polarization of two types of WR stars (WR93b, WR102). To numerically model the winds of WR stars we need to know the stellar parameters and the CAK parameters of the line force.

For the stellar parameters, we adopted the data from Tramper et al. (2015) and Stevance et al. (2018) as shown in Table 6.1. However, for CAK parameters there has not been any precedent calculation for these two stars. We selected such values of α and k, to fit the observational terminal velocity and the mass loss rate. The obtained values of α, k, and δ are given in Table 6.2.

Table 6.1: Adopted stellar and wind parameters of studied WR stars.

WR	$\log(L_\star/L_\odot)$	$T_\star$ (kK)	$R_\star$ ($R_\odot$)	$M_\star$ ($M_\odot$)	v_∞ (km s^{-1})	$\log(\dot{M}/1\,M_\odot\,\mathrm{yr}^{-1})$
WR93b	5.30	160	0.58	7.1	5000	-5
WR102	5.45	210	0.39	7.0	5000	-4.92

Table 6.2: Adopted CAK parameters for WR stars.

Star	α	k	δ
WR93b	0.52	0.61	0
WR102	0.52	0.61	0

We implemented the stellar parameters in the code and we kept the same configuration of the boundary conditions as for Be star. It is worth noting that we were able to find the best fit for the mass loss and the terminal velocity for nonzero of δ, however, when we run the simulation with rotation, we found the non-physical structure of the density and the other hydrodynamic parameters.

The corresponding mass loss rate to the selected CAK parameters is $5.8\times10^{-7}M_\odot\mathrm{yr}^{-1}$ for WR93b and $4.7\times10^{-7}M_\odot\mathrm{yr}^{-1}$ for WR102, which is different from the one given in Table 6.1. For quantitative analysis, such as polarization, we need to multiply the density by the ratio of the observed mass loss to the fitted values from the numerical simulation, assuming the linear dependence of the density on the mass loss rate. The ratio is found to be 17 and 24, for WR93b and WR102, respectively. For the terminal velocity we found that $v_\infty = 6000 \mathrm{km.s}^{-1}$ for WR93b, and $v_\infty = 8000 \mathrm{km.s}^{-1}$ for WR102.

We run the model for different rotational velocities and this lead to wind compression effect as proposed by Bjorkman and Cassinelli (1993) and Ignace, Cassinelli, and Bjorkman (1996). As for Be star, there is a density enhancement at the equatorial regions, as discussed in the work of Ignace, Cassinelli, and Bjorkman (1996) for WR star the is a formation of wind-compressed zone (WCZ) due to just low stream at the equator.

6.1.3 Low metallicity stars

Metal-poor stars, also called low-metallicity stars, have reduced amounts of elements heavier than helium. These stars exhibit transparent winds due to decreased mass loss (Kubátová et al., 2019). To simulate the wind dynamics of such stars, we require knowledge of their stellar parameters and CAK line force parameters. As in the case of WR stars, no prior information on CAK parameters was found, necessitating the optimization process we performed in the previous section. Table 6.3 presents the stellar parameters for various stars.

Utilizing these parameters, we established the code setup, maintaining the same configurations as those for the preceding stars. Table 6.4 provides a summary of the optimized CAK line force parameters based on the given mass loss rate and terminal velocity.

Table 6.3: Stellar parameter of low metallicity (Kubátová et al., 2019), the mass loss rates, based on the code of Krtička and Kubát (2017), are from private communication with Krtička.

Star	$\log(T_{\rm eff})$ (K)	$\log L_\star$ $(L_\odot)$	$R_\star$ $(R_\odot)$	$M_\star$ $(M_\odot)$	$\log(\dot{M})$ $(M_\odot \mathrm{yr}^{-1})$	v_∞ $(\mathrm{km.s}^{-1})$
CheB(T-5)	5.08	5.67	1.55	16.8	-7.02	2040
0.28(T-6)	4.74	5.75	8.14	58.9	-8.09	1340
0.75(T-8)	4.84	6.13	8.08	58.3	-7.31	970
0.98(T-9)	4.92	6.29	6.68	55.3	-6.09	750
CheB(T-10)	5.14	6.34	2.6	49.4	-5.79	3220
0.28(T-11)	4.76	6.29	13.71	130.8	-7.26	1260
0.50(T-12)	4.79	6.42	14.26	129.9	-7.85	930
0.75(T-13)	4.84	6.57	13.63	126.8	-6.31	1530
0.98(T-14)	4.93	6.96	10.18	112.5	-5.85	2420
CheB(T-15)	5.14	6.68	3.82	93.3	-5.01	520

As for previous stars, we ran the code for different rotational velocities, we found a fair agreement comparing the semi-analytical model of BC. We note those stars are similar to O stars so the compressed material at the equator can be classified as WCD.

Table 6.4: CAK line force parameters of low metallicity stars.

Star	α	k	δ
CheB(T-5)	0.396	0.141	0.12
0.28(T-6)	0.43	0.143	0
0.75(T-8)	0.34	0.2	0.16
0.98(T-9)	0.28	0.22	0.16
CheB(T-10)	0.34	0.23	0.13
0.28(T-11)	0.358	0.2	0
0.50(T-12)	0.36	0.15	0
0.75(T-13)	0.37	0.15	0
0.98(T-14)	0.36	0.1	0
CheB(T-15)	0.2	0.26	0.05

6.2 Effect of gravity darkening and nonradial forces

In the previous section, we followed the assumption of BC, and we modeled dynamically the WCD. The results showed a good agreement between theoretical predictions and 2.5D numerical simulations. It is worth noting that in this model, we only considered the radial component of the radiative force. However, in reality, the radiative force has three directional components $\boldsymbol{f}_{\text{rad}} = (f_r, f_\theta, f_\phi)$. We show in the following section the effect of radial force, non-radial forces and gravity darkening.

As in the previous section, we derive the time-dependent numerical hydrodynamic simulation for a set of massive stars. The simulations here are based on the method and code described by Cranmer and Owocki (1995) and Owocki, Cranmer, and Gayley (1996), where line force is expressed in all three components, and the boundary is controlled by the effect of gravity darkening model using von Zeipel theorem described in Chap 3.

The boundary conditions were similar to those in the previous section, where we set a fixed density of a lower boundary in the radial direction to maintain the supersonic wind and the velocity was set to extrapolate (inflow). For the upper boundary, all variables were set to outflow. We set a reflective boundary conditions at the latitudinal direction.

We will discuss two models that are representative of the wind of massive stars: the WR star which has an optically thick wind, low-metallicity and VFTS stars which have optically thin wind. Our simulation of Be stars was conducted to compare it to the existing literature, specifically the research done by Owocki, Cranmer, and Gayley (1996). Figure 6.3 displays the contour plot of the density of the Be star.

For quantitative analysis needed to compute the polarization we have extended the radius r from $1R_\star$ up to $10R_\star$, subdivided into 320 grid points to get a fine structure, and we reduced the latitudinal grid to 100 grid points to reduce computational time.

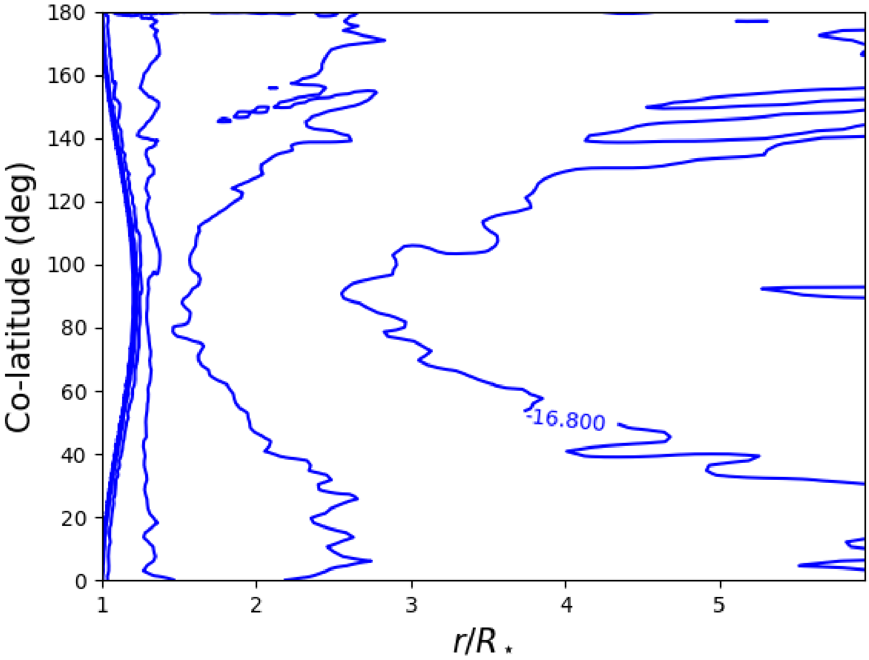

Figure 6.3: Density contours of stellar wind of Be star as a function of radius and co-latitude θ, log scaled spaced by 0.8 dex, for rotation $V_{\rm rot}$ = 350 km.s^{-1}, the denoted contour correspond to $\log(\rho/(1{\rm g.cm}^{-3})) = -16.8$.

6.2.1 Wolf Rayet stars

We performed simulations with varying rotational speeds of the two stars (WR93b and WR102) as described in the previous section. Figure 6.4 depicts the wind density pattern, taking into account the influence of non-radial line forces and gravity darkening. This particular illustration represents WR93b with a rotational velocity of 1100 km.s^{-1}, which is 63% of the critical rotation speed 1736 km.s^{-1}. In this particular case, it is interesting to note that there is no presence of a disk, and the density in the equatorial region is lower compared to the polar regions. This observation contradicts the prediction of the WCD model proposed by Bjorkman and Cassinelli (1993). However, it aligns with the findings of Owocki, Cranmer, and Gayley (1996), who found an inhibition of the WCD in Be stars. This discrepancy raises questions about the mechanisms that govern the formation and presence of disks in massive stars.

In our investigation of WR102, we observed comparable results. Throughout our extensive simulations, we examined rotation rates reaching up to 85% of the critical speed. However, we did encounter numerical instability concerns near the equator when the rotation rate exceeded 75%.

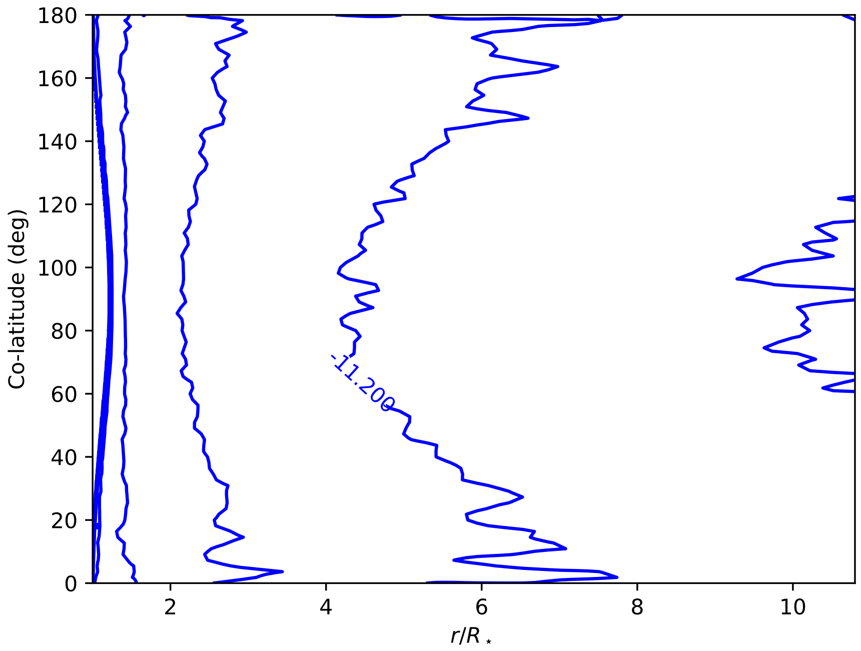

Figure 6.4: Density contours of stellar wind of WR93b as a function of radius and co-latitude θ, log scaled spaced by 0.8 dex, for rotation V_{rot} = 1100 km.s^{-1}, the denoted contour correspond to $\log(\rho/(1\text{g.cm}^{-3})) = -11.2$.

We observe that the stronger (weaker) flux from the poles (equator) significantly influences the mass flux, leading to an increase (decrease) in mass loss and local wind density. Additionally, the presence of stellar oblateness causes the radiative force to point away from the equator and in the opposite direction of rotation (Cranmer and Owocki, 1995; Owocki, Cranmer, and Gayley, 1996). As a result, there is a net deflection of wind streamlines towards the poles. This contradicts the "wind-compressed disk" the model proposed by BC.

6.2.2 Low metallicity stars

In our simulation, we considered the rotational velocities mentioned in the study conducted by Kubátová et al. (2019). The rotation rate varies among the stars (see Table.6.5), with some, like T6 and T14, having a rotation speed of about 40% of the critical rotation. Others, such as T5 and T12, exhibit rotational velocities of approximately 85% of the critical rotation.

Table 6.5: Rotational velocity ($v_{\rm rot}$) from Kubátová et al. (2019), and computed critical velocity using Eq 6.2 for different stars, $\bar{\omega}$ is the ratio of rotational velocity to the critical velocity.

Star	$v_{\rm rot}$(km.s^{-1})	$v_{\rm crit}$(km.s^{-1})	$\bar{\omega}$ (%)
CheB(T-5)	994	1173,63	84,69
0.28(T-6)	421	958,93	43,90
0.75(T-8)	422	957,57	44,06
0.98(T-9)	404	1025,69	39,38
CheB(T-10)	755	1553,89	48,58
0.28(T-11)	905	1101,1	82,19
0.50(T-12)	925	1075,94	85,97
0.75(T-13)	820	1087,31	75,41
0.98(T-14)	520	1185,07	43,87
CheB(T-15)	587	1761,78	33,31

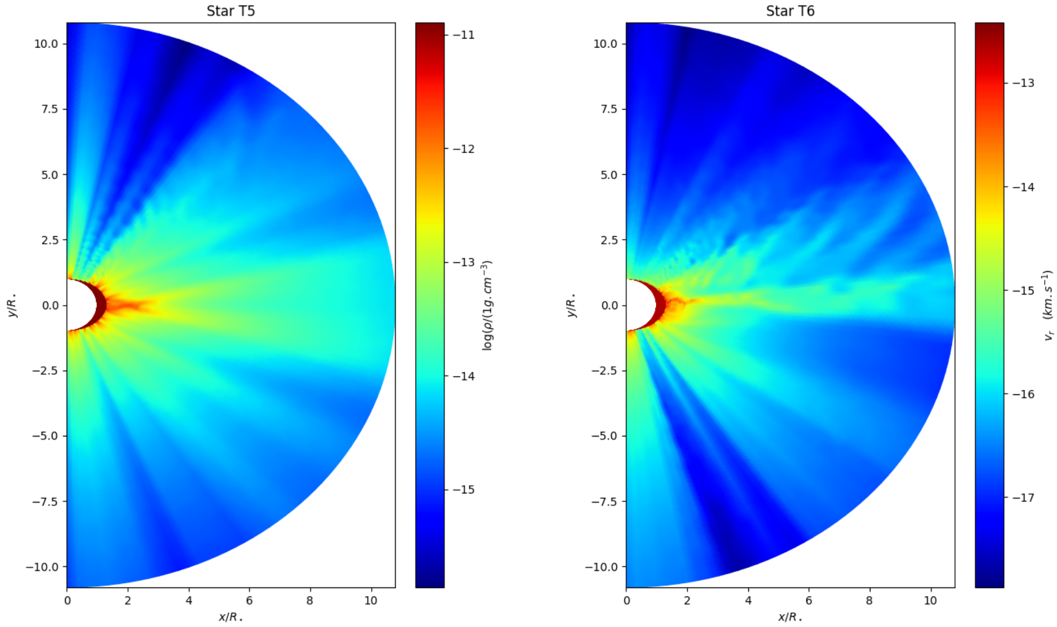

Figure 6.5: Surface plot in logarithmic scale of the density for the stars:(*left*) T5 with $v_{\rm rot}$ = 994 km/s , (*right*) T6. $v_{\rm rot}$ = 810 km/s.

We have performed hydrodynamic simulations for all the rotational velocities stated in Table 6.5. Interestingly, we found that stars T5 (Fig 6.5), T11, and T12 (Fig 6.8), which have rotational velocities exceeding 80% of the critical velocity, exhibited a density enhancement in their equatorial regions. This goes against our initial expectation of the inhibition of the WCD at high rotational velocities. To further investigate this phenomenon, we decided to increase the rotation of the stars to reach a rotational velocity of 85% of the critical velocity.

From the results shown in Fig 6.7, it is evident that the increased rotation did not lead to the formation of a disk for the stars T8 and T9. Additionally, the density at the equator was reduced for these stars. Similar results were observed for the stars T13, T14, and T15, where no disk formation occurred and there was a decrease in density at the equator. However, for the star T6, T10, and T13, a density contrast was observed at the equator, indicating the potential formation of a disk (Fig 6.5).

Figure 6.6 shows the radial velocity and latitudinal velocity for the star T6. This particular description offers valuable insights into the overall structure of the flow pattern. It consists of two key components: a fast radial flow at the pole, characterized by low density (Fig 6.5), and a slower outflow that is denser and primarily located within the equatorial disk. It is important to note that the variables ρ, v_r, and v_ϕ exhibit symmetry around the equator, while the velocity v_θ exhibits antisymmetry (Owocki, Cranmer, and Blondin, 1994). This asymmetry is a result of the compressional flow directed towards the equator, which consequently leads to the heightened density and formation of the disk. Table 6.6 presents an expanded summary of the formation process of an outflowing equatorial disk for each star.

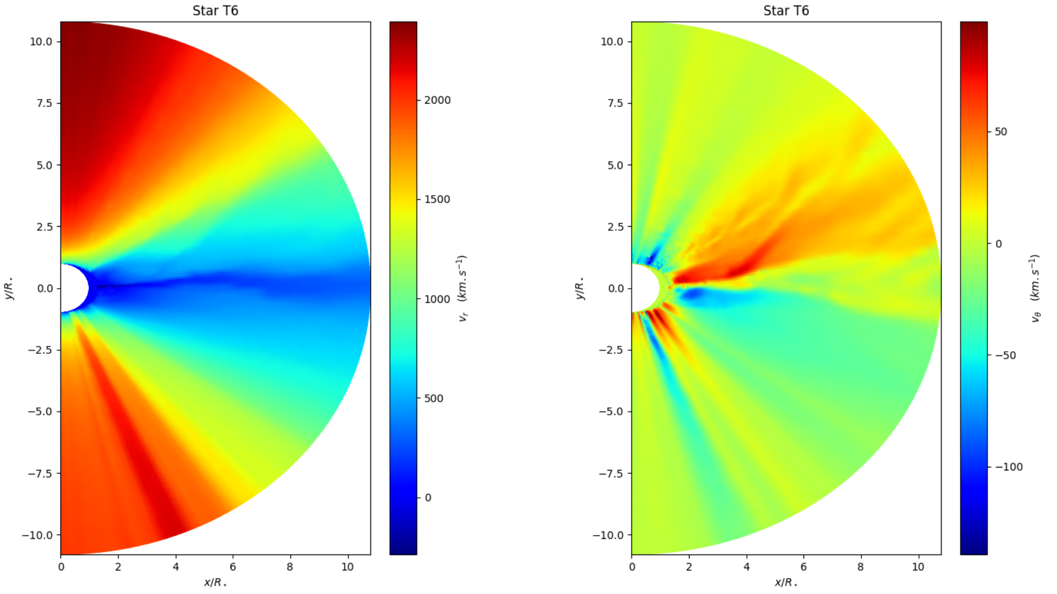

Figure 6.6: Surface plot for radial velocity (*left*), and latitudinal velocity (*right*) for the star T6 with $v_{\rm rot} = 810$ km/s.

The figures clearly show the existence of stripes, a phenomenon that can be explained by the particular staircasing boundary conditions that were considered. Additionally, the snapshots were taken during a time frame of 10^6 to 10^7 s for certain stars, and the steady solution has not been fully achieved yet.

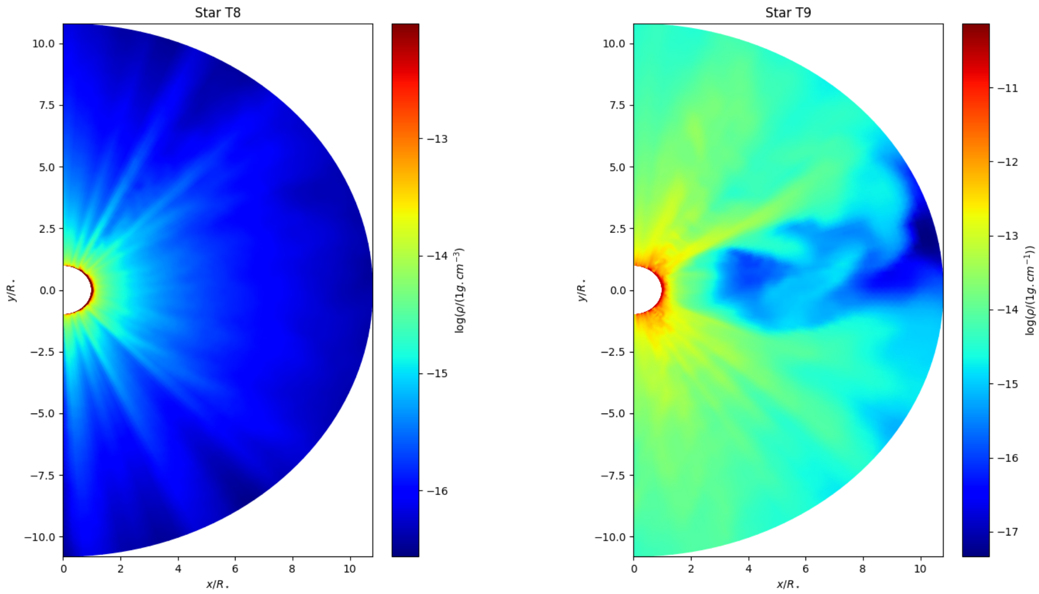

Figure 6.7: Surface plot in logarithmic scale of the density for the stars: (*left*) T8 with $v_{\rm rot}$ = 810 km/s, (*right*) T9 with $v_{\rm rot}$ = 910 km/s.

Table 6.6: Summary of the presence of WCD in low metallicy stars.

Star	$v_{\rm rot}$(km.s^{-1})	WCD
CheB(T-5)	994	yes
0.28(T-6)	810	yes
0.75(T-8)	810	no
0.98(T-9)	630	no
CheB(T-10)	1330	yes
0.28(T-11)	905	yes
0.50(T-12)	925	yes
0.75(T-13)	920	yes
0.98(T-14)	1000	no
CheB(T-15)	1510	no

These findings suggest that the rotational effects on disk formation and density distribution can vary among different stars. In a previous study by Curé (2004) and Curé, Rial, and Cidale (2005), they observed an outflowing disk with a rotation rate higher than 70%. However, their analysis focused on the location of the critical point (Curé, 2004), and the bi-stability jump (Curé, Rial, and Cidale, 2005), which was not considered in the current investigation. Additionally, they neglected to include the effect of gravity darkening, an aspect that we have considered in our research.

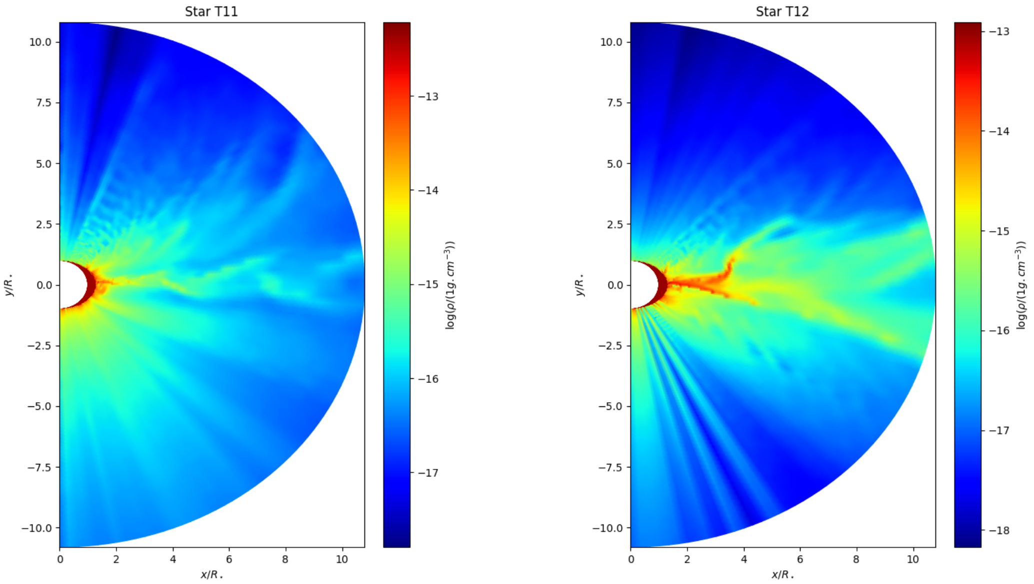

Figure 6.8: Surface plot in logarithmic scale of the density for the stars: (*left*) T11 with $v_{\rm rot}$ = 905 km/s, (*right*) T12 with $v_{\rm rot}$ = 925 km/s.

Another effect that could be cause of the disk formation is the viscosity. The idea that the near-critical rotation of Be stars leads to the formation of disks has been proposed by Townsend, Owocki, and Howarth (2004). According to this notion, these disks are likely formed through the centrifugal ejection of material near the equatorial surface, resulting in a Keplerian orbit. This ejected material then undergoes an outward diffusion of mass and angular momentum, leading to the formation of a radially extended viscous decretion disk (Lee, Osaki, and Saio, 1991). In contrast to the well-understood process of radiative lifting of stellar wind, which occurs due to a deep gravitational potential, decretion represents a different mechanism where material spills over from a critical surface, similar to Roche-Lobe overflow in mass-exchange binaries. While wind driving is comparable to suction through a straw from a partly full glass, with mass flux depending on the strength of the suction force, centrifugal decretion is more like the spillage from a nearly full glass Owocki (2012). Small perturbations can cause random and chaotic mass overflow. Instead of relying on external driving forces, the overall level of centrifugal mass loss depends on the internal mechanisms that maintain the stellar rotation near critical.

6.2.3 VLT-FLAMES Tarantula Survey (VFTS)

The VLT-FLAMES Tarantula Survey (VFTS) is a project conducted by the European Southern Observatory (ESO) aiming to gather extensive spectroscopic data on a large number of massive stars in the 30 Doradus region of the Large Magellanic Cloud (LMC). This survey involves the use of the Very Large Telescope (VLT) and the FLAMES instrument to observe these stars multiple times over some time (Evans et al., 2011).

According to the spectroscopic observations conducted by Shepard et al. (2020), they discovered some interesting features in the stars VFTS 102 and VFTS285. In the case of VFTS102, they detected a double-peaked H_α profile, suggesting a complex and possibly inhomogeneous wind outflow. On the other hand, for VFTS 285, they observed fast wind outflow in the Nv lines and a slower wind component in the overall spectrum.

In the previous section, we utilized a time-dependent numerical hydrodynamics simulation to determine the wind structure of different stars. Similar to our approach with previous stars, we required the stellar parameters for VFTS to optimize the CAK line force. These stellar parameters, essential for our calculations, are provided in Table 6.7.

Table 6.7: Stellar parameters of VFTS stars (Shepard et al., 2020).

Star	$\log(T_{\text{eff}})$ (K)	$\log L_\star$ $(L_\odot)$	$R_\star$ $(R_\odot)$	$M_\star$ $(M_\odot)$	$\log(\dot{M})$ $(M_\odot \text{yr}^{-1})$
VFTS 102	4.55	5.0	8.17	18	...
VFTS 285	4.53	5.0	6.6	20	...

By applying our methodology, we were able to obtain the CAK parameters for the two stars, which are summarized in Table 6.8. These CAK parameters represent crucial information that helps us understand and model the wind behavior of the VFTS stars.

Table 6.8: CAK line force parameters

Star	α	k	δ
VFTS 102	0.52	0.61	0.166
VFTS 285	0.51	0.61	0.166

In this case, we chose to restrict our numerical simulation to a rotational velocity of 100% of the critical velocity. This decision was made to directly compare our simulation results with the observations conducted by Shepard et al. (2020). The reported rotational velocities for VFTS 285 and VFTS 102 were recorded as 609 and 610 km/s, respectively. These values indicate that these stars are rotating at their critical speed, making them significant observations in the study of stellar rotation.

In Figure 6.9, we can observe a surface plot representing the density and radial velocity of the star VFTS 285. The plot provides valuable insights into the star's dynamics. Specifically, we notice a density enhancement in the star's equatorial regions, indicating a relatively slower outflow of material in those areas. On the other hand, the polar regions demonstrate lower density with a faster outflow of material.

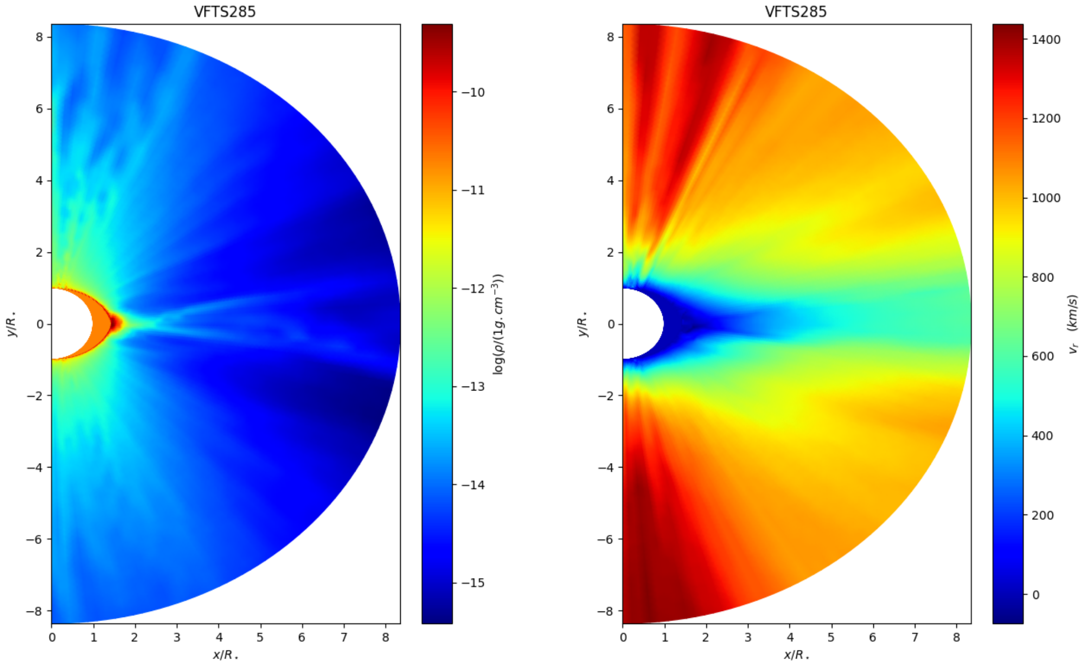

Figure 6.9: Surface plot for the density (*left*) and radial velocity (*right*) for VFTS 285 star, at the critical rotation of 609 km/s.

The density distribution observed in VFTS 285, characterized by an equatorial density enhancement and a polar density decrease align with the findings reported by Shepard et al. (2020). The researchers suggested a two-wind regime based on the presence of the two elements N_v and $\mathrm{Si}_I V$. This distinction is evident in the image, where a density enhancement is observed at the equator, while some dense material is still present around the polar regions. This observation supports the hypothesis that high rotation rates can lead to an expansion of the equatorial radius, resulting in the observed density distribution.

For the star VFTS 102, the simulation results demonstrate the presence of an equatorial outflowing disk, thus supporting the observation of a double peak of H_α (Shepard et al., 2020). This alignment between the simulation and observation provides compelling evidence for the existence of a disk around the star, with material flowing outward in the equatorial plane.

It is interesting to note that in our simulations, we observed a reduction in density at the equator rather than an enhancement, when simulating with a rotation speed less than 90% of the critical value. This aligns with the inhibition of WCD by Owocki, Cranmer, and Gayley (1996).

Shepard et al. (2022) have recently reported a new critical velocity for VFTS 102 and VFTS 285 stars. According to their study, the critical velocity for VTFTS 285 is calculated to be 648 km/s, while for VFTS 102, it is determined to be 649 km/s. This finding will be a topic of discussion in our forthcoming project.

6.3 Other codes

The VH1 code has limitations as it only considers the hydrodynamic model equation and does not account for magnetic fields. However, several other codes have been developed and are commonly used in astrophysics. Some of the currently available codes are FLASH (Fryxell et al., 2000), ATHENA++ (Stone et al., 2020), and PLUTO (Mignone et al., 2007). We implemented the radiative force in all of these codes, and the result found in 1D agreed with the literature, however, in 2D we encountered some numerical issues including the limitation of some codes compared to others. For instance, in the FLASH code, the effect of rotation is not included in the PPM split solver, since it is required by the spherical geometry. We choose to continue with PLUTO due to its universality. Unlike VH1, PLUTO requires that the variables be in dimensionless units (code units), where we scaled the density by the values $\rho_0 = 2.10^{-13}$ g/cm^3, the velocity by $v_0 = 10^5$ km/s, and the length by stellar radius $L_0 = R_\star$.

To replicate the setup used in VH1, we have made some modifications to the grid and boundary conditions. Firstly, we have extended the radial domain up to 10 times the stellar radius with a total of 200 grid points. Additionally, we have divided the colatitude into 100 grid points. We focused specifically on the radial component of the radiative force, and we selected a spherical geometry case as the basis for our model.

To ensure proper boundary conditions, we have implemented reflective boundaries in both the upper and lower sides of the latitudinal direction. For the upper boundary in the radial direction, we have set an outflow boundary. Meanwhile, at the lower boundary, we have fixed the wind density and set the radial velocity to be a subsonic inflow. After several tests, we determined that setting the latitudinal velocity to zero yielded the best results. Additionally, we have maintained solid body rotation for the azimuthal velocity. These adjustments aimed to replicate the same setup as VH1 while ensuring accuracy and reliability in our simulations.

To establish the initial conditions, we assign a wind density value of one and apply the beta velocity law for the radial velocity. We assume zero latitudinal velocity and adopt the Keplerian rotation law for the azimuthal velocity.

Figure 6.10 shows the surface plot of the density and radial velocity. The result obtained from the simulations bears a resemblance to the findings depicted in Fig 6.1. However, there are minor variations that can be attributed to the setup of the lower boundary conditions in the radial direction possibly influenced by the latitudinal velocity. To enhance the accuracy of the simulations, additional analysis and tests are required.

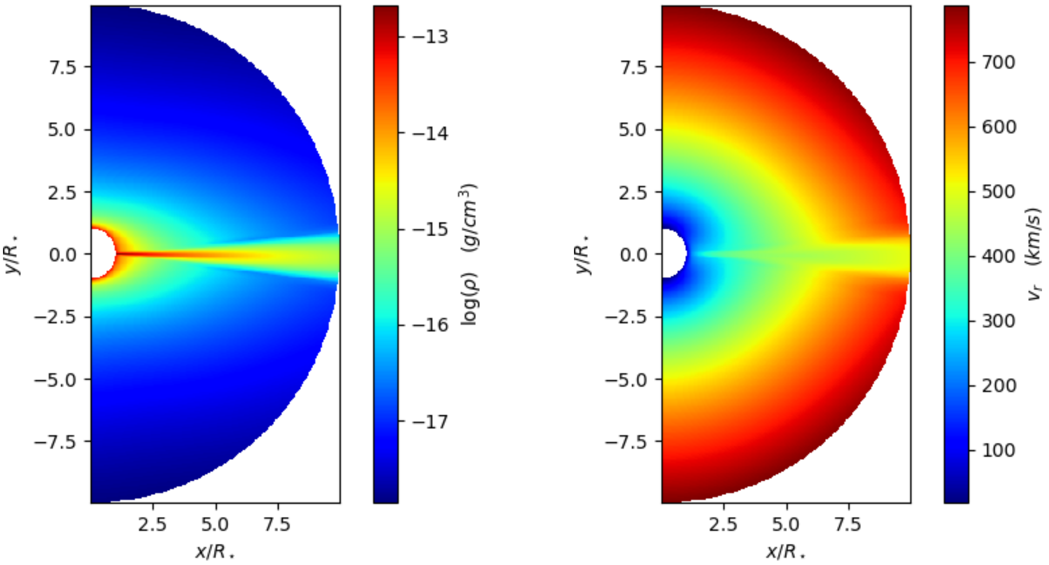

Figure 6.10: Surface plot of the density in log scale (*left*), and the radial velocity (*right*) of Be star from PLUTO code.

Chapter 7

Polarization due to electron scattering

In the atmospheres of massive stars, electron scattering leads to polarization. The process results in light waves becoming aligned along specific directions. Instruments like spectropolarimeters utilize this polarization by detecting it and measuring light intensity across various wavelengths.

The polarization of light due to electron scattering in massive stars was first predicted by Chandrasekhar in the 1940s (Chang, Jiang, and Lin, 2013). He calculated that a substantial linear polarization would occur at the stellar limb, meaning that the light waves would be aligned in a particular direction. The root of this divergence lies in the dissymmetry that pervades the limpid milieu enveloping individual stars, an imbalance brought about by a binary partner or other extraneous influences.

Electron scattering in massive stars can produce light polarization that is subject to modification by a weak magnetic field, known as the Hanle effect (Cotton et al., 2017). The strength of this field determines how much change occurs. Polarized light caused by electron scattering has other benefits including studying properties like stellar winds and local medium characteristics while tracking star motions for more comprehension regarding its atmosphere structure or physical processes happening within it. With such study, astronomers may explore the magnetic fields surrounding celestial objects effectively via the use of tools provided by the Hanle effect among others available to them today with great results seen so far!

7.1 Continuum polarization

The theoretical model of the polarized radiation due to electron scattering depends on the integral of the electron number density over the volume of scattering (Brown and McLean, 1977). The analytical expression of the polarization from Thomson scattering developed by Brown and McLean (1977) has been refined to include the effect of finite stellar structure $D(r)$ (called depolarization effect) by Cassinelli, Nordsieck, and Murison (1987), using this expression, the polarization due to an axisymmetric density distribution is given by

$$P_R = \frac{3}{16}\sigma_T \sin^2 i \int_{r_1}^{r_2} \int_{\mu_1}^{\mu_2} n_e(r,\mu)(1-3\mu^2)D(r)drd\mu \tag{7.1}$$

where σ_T is Thomson scattering cross section, i represents the inclination angle, n_e is the electron number density, r is the radius, and $\mu = \cos\theta$ is the cosine of the colatitude θ; the integral is carried out over the surface as shown in Fig 7.1.

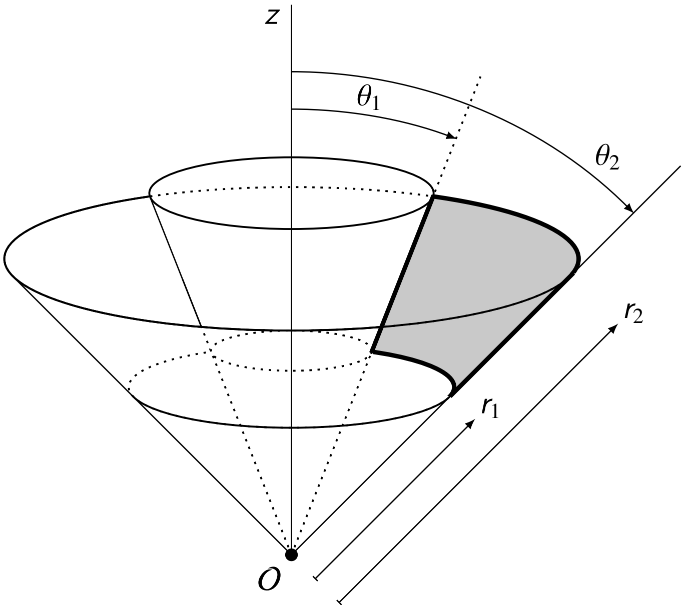

Figure 7.1: Plane of integration in spherical geometry adopted from Brown, Ignace, and Cassinelli (2000).

7.2 Single scattering polarization

The analytical expression of the polarization Eq 7.1 is intended for optically thin electron scattering. Since the numerical hydrodynamic simulation includes stair casing at lower boundary conditions in radial coordinate, to avoid this effect that could lead to an overestimate of the polarization, we choose to integrate from the region where we ensure that the optical depth τ is less than one, we applied Eq 7.1 to compute the polarization for two typical WR stars, where the integral is computed from the $r_1 = 1.2R_\star$.

In the context of observations, Stevance et al. (2018) investigated the dependence of the intrinsic polarization on the stellar rotation using the simplified WCD model by Ignace, Cassinelli, and Bjorkman (1996). Figure 7.2 shows a comparison of the polarization computed assuming the simplified model (WCD), oblate density distribution from numerical simulation due to the effect of radial force only (hydro with radial), and prolate density structure due to the effect of non-radial forces and gravity darkening (hydro with full model) of the two WR stars (WR93, WR102) at a rotation speed $v_{\rm rot} = 900$ km.s^{-1}.

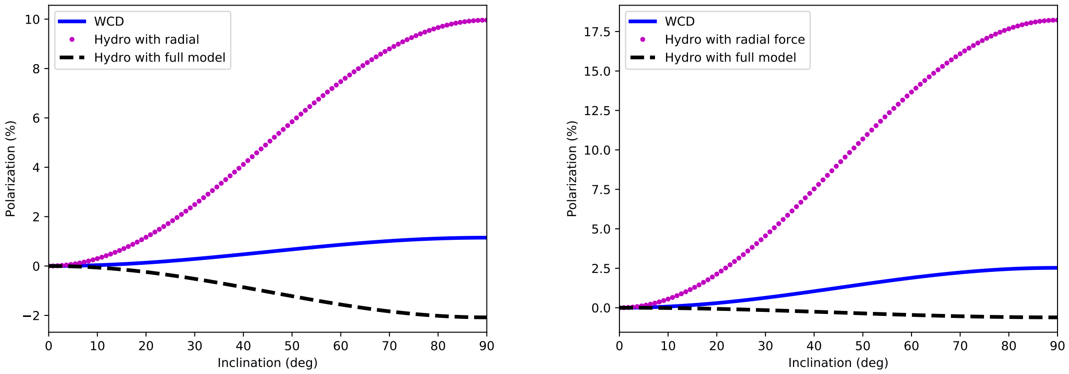

Figure 7.2: Comparison of the percentage polarization as a function of the inclination between the analytical model of WCD (based on the model of Ignace, Cassinelli, and Bjorkman 1996), numerical hydrodynamic model including radial force only (hydro with radial), and complete hydrodynamic with nonradial forces and gravity darkening, for a rotational velocity $v_{\rm rot} = 900$ km.s^{-1} for the two stars; *Left*; WR93b, *Right*; WR102.

The polarization signature depends on geometry. It is clear from fig 7.2 for a disk-like geometry the polarization is positive, when the geometry changes to jet-like geometry it becomes negative. Another effect that can be seen due to the inclination angle is that when the system is viewed pole-on ($i = 0$), the polarization vanishes, indicating that the matter is symmetric concerning the direction of viewing. Changing the observation angle and viewing edge-on (at the equator $i = 90 deg$) we can see the maximum polarization is reached. The hydrodynamic model using radial force only showed a higher value of polarization compared to WCD, this is due to the fact that the matter is confined to the equatorial regions, and comparable absolute values can be seen between WCD and the complete model.

To study the effect of rotation on polarization we limited ourselves to the complete hydrodynamic model, where the density is given as a prolate distribution. Figure 7.3 shows the variation of linear polarization as a function of the inclination for different rotational velocities.

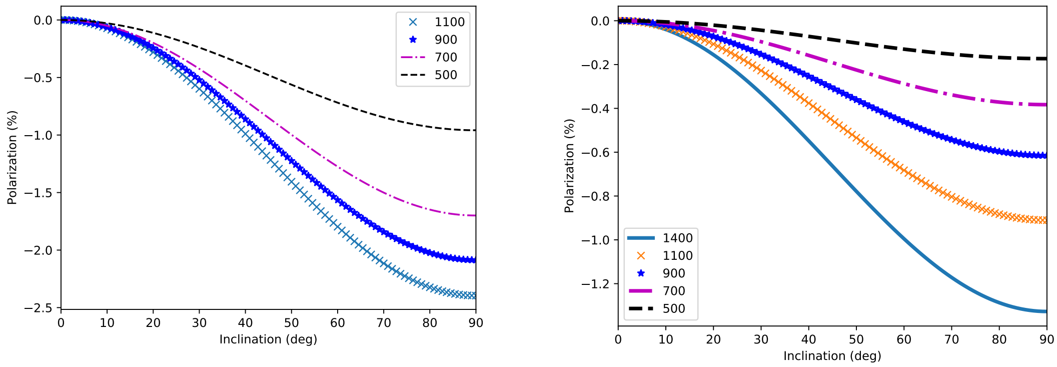

Figure 7.3: Percentage polarization as a function of inclination, for different rotational velocities in unit of km s^{-1} as labeled, using complete hydrodynamic simulation; *Left*; WR93b, *Right*; WR102

We intended to compare our model with the model of Stevance et al. (2018), where the determined the upper limit for the rotational velocities according to the polarimetric observations. However, we faced more complex computational challenges, since we were not able to make hydrodynamic modeling at low rotational speed (< 500 km s^{-1}), as we have seen non-physical structure for the density distribution using both cases (radial and complete model). To determine the upper limits for the rotational velocity, we used a logarithmic least square fitting of the polarization obtained by the complete model. Table.7.1 shows a comparison between our model using the complete model and the limits obtained by Stevance et al. (2018). The angular momentum is calculated using the formula $j = v_{rot} * R_\star$. Comparing the results of the angular in Tab.7.1 with the derived threshold ($j \geq 3.10^{16}$cm^2.s^{-1}) by MacFadyen and Woosley (1999), we easily see that the obtained limits exceed the threshold, as a result, the studied WR stars qualify as a progenitor of long Gamma-Ray burst (LGRB). Our model agrees well with the results from observation using spectropolarimetry (Stevance et al., 2018) and using the photometry by Gräfener et al. (2012).

Table 7.1: Comparison between the fitted maximum observationally allowed rotational velocity (in km s^{-1}) in our model and the model of Stevance et al. 2018. P_R is the upper limit of the polarization. The last column gives the maximum specific angular momentum determined from the maximum allowed rotational velocity.

WR	P_R (%, observation)	$v_{\rm rot}$(km/s) (Stevance's model)	v_{rot}(km/s) (Current model)	$\log(j/1{\rm cm}^2{\rm s}^{-1})$
93b	0.077	324	277	17.88
102	0.057	234	444	17.85

7.3 Effect of multiple-scattering

In this section, we apply the Monte Carlo method for computing the polarization of the emergent intensity due to electron scattering in the wind. Stokes parameters were computed using 3D Monte Carlo radiative transfer (MCRT) code HYPERION (Robitaille, 2011). The code is parallelized and solves the radiative transfer equation in different sets of geometry, including Cartesian, cylindrical, polar, and spherical. In this work, we will use the spherical geometry.

Our simulation focuses on calculating the polarization resulting from electron scattering alone. The simulation involves tracking the movement of photon packets emitted from a central radiation source. In section 7.2, we utilized the outcomes derived from hydrodynamic simulation to calculate the polarization. The framework we employed was based on the simplified model of the CAK line force for an optical thin wind. However, it is important to note that the wind of WR exhibits optical thickness, implying the presence of outer envelopes that envelop the atmosphere of WR stars. An analytical expression of the density in fast rotating stars was developed by Dwarkadas and Owocki (2002), which takes into account the gravity-darkening effect and considers the distribution of mass flux in the simulation. This expression reveals that the mass flux is more pronounced at the polar regions and gradually diminishes towards the equator. This density distribution is an essential factor in determining the polarization and is given by

$$\rho(\bar{\omega},\theta) = \rho_0(r)\sqrt{1-\bar{\omega}^2\sin^2\theta}. \tag{7.2}$$

In this study, we used the equation $\rho_0(r) = \dot{M}/(4\pi v(r) r^2)$ to calculate the density distribution in our computational domain. This equation takes into account the mass loss rate $\dot{M}$, the radial distance r, and the rotation ratio $\bar{\omega}$ which compares the rotational velocity to the critical velocity. Additionally, we incorporated the β velocity law, denoted as $v(r)$, which describes how the velocity changes with distance.

To represent the stars in our simulation, we treated them as point sources located at the center of the computational domain. These stars were assigned specific luminosities and effective temperatures (see Table 6.1). By combining these parameters with the density distribution equation, we were able to model the behavior and characteristics of the stars in our study. To enhance accuracy, we have adjusted the photon numbers to be 10^7 for both imaging and ray-tracing purposes. We have conducted a comparison between the output of the Monte Carlo simulation with the single scattering model (Eq 7.1), and the single scattering model incorporating an attenuation factor. By introducing the attenuation factor $e^{-\tau}$, we can express the polarization equation as follows (McLean, 1979; Friend and Cassinelli, 1986)

$$P_R = \frac{3}{16}\sigma_T \sin^2 i \int_{r_1}^{r_2}\int_{\mu_1}^{\mu_2} n_e(r,\mu)(1-3\mu^2)e^{-\tau}D(r)\,dr\,d\mu, \tag{7.3}$$

where τ is the optical depth for absorption.

7.3.1 Effect of rotation

The results of a comparison between the single scattering model, the single scattering model with attenuation, and the multiple scattering model are presented in Fig 7.4. The comparison reveals that the two models agree reasonably well up to a 50% rotation of the critical value. However, at higher rotation speeds, the polarization induced by multiple scattering exhibits significant deviations from the single scattering model.

A closer examination of the polarization data reveals that the effect of multiple scattering is quite pronounced at inclination angles of 40 and 60 degrees. Specifically, the degree of polarization was found to increase significantly at 40 degrees, followed by a sharp decrease at 60 degrees, as shown in Fig 7.5. This observation indicates that when the system is observed at high inclinations, the scattered light has to pass through a larger amount of gas before it leaves the system. Due to this, a portion of the polarized light gets absorbed, leading to a decrease in the overall polarization level. This effect is seen also in the Monte Carlo simulations of polarization by Wood et al. (1996) and Halonen and Jones (2013).

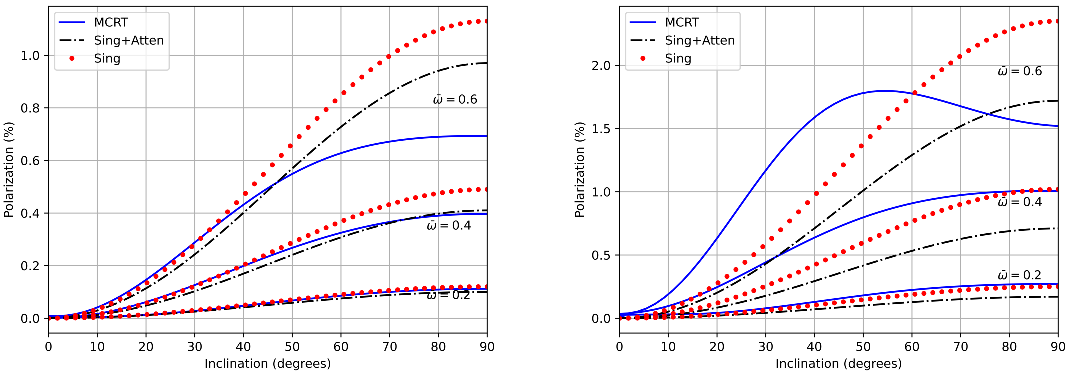

Figure 7.4: Polarization as a function of the inclination, due to the effect of single scattering (sing), single scattering with attenuation (Sing+Atten), and multiple scattering (MCRT) for different rotation rates: *(left)* for WR93b, *(right)* for WR102.

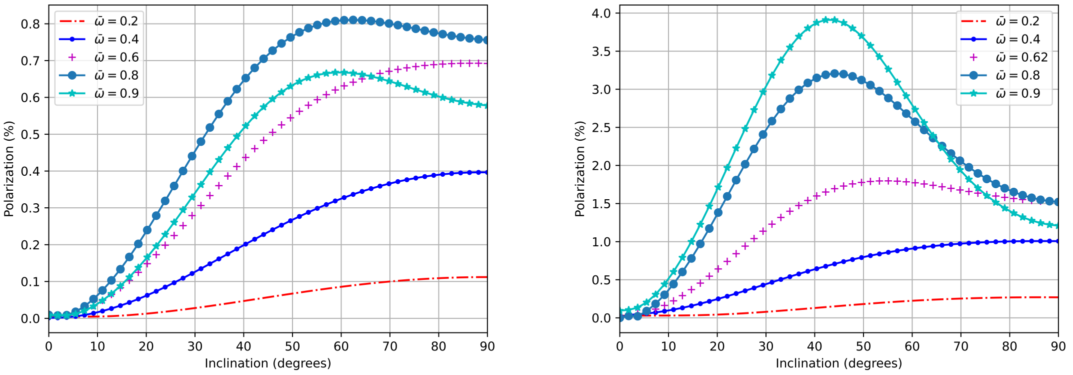

Figure 7.5: Polarization as a function of inclination for different rotational velocities from multiple-scattering: *(left)* for WR93b, *(right)* for WR102.

7.3.2 Effect of mass loss

The polarization properties of Wolf Rayet stars are influenced by various factors, including the mass loss rate. As the mass loss rate of a Wolf Rayet star changes, the optical depth of its stellar wind also changes, leading to variations in the polarization of the scattered light.

To illustrate this relationship, a plot of the polarization as a function of inclination was created for different values of mass loss. As shown in Fig 7.6, the degree of polarization increases with increasing mass loss rate. This effect is due to the fact that higher mass loss rates result in a greater number of scattering particles in the wind, leading to a higher degree of polarization.

Reducing the mass loss rate will reduce the number density will decrease, resulting in a decrease in the optical depth. This reduction in optical depth, denoted as $\tau << 1$, can be approximated using Taylor expansion as $e^{-\tau} \approx 1 - \tau$. Consequently, the attenuation factor will no longer have an impact on polarization, unlike its effect on high mass loss.

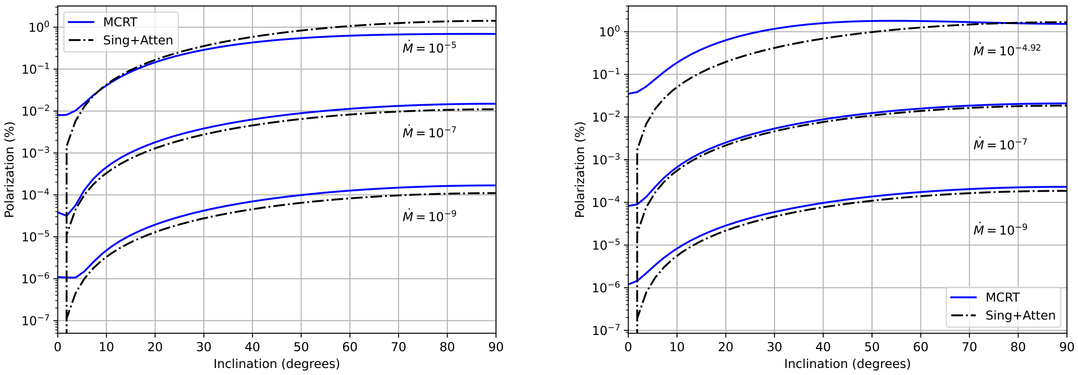

Figure 7.6: Polarization, in log scale, as a function of inclination for different mass loss in unit $M_\odot$/yr from single with attenuation and multiple-scattering at rotation rate $\bar{\omega} = 0.6$.

Chapter 8

Conclusion and future work

8.1 Current work overview

The purpose of this work has been to model numerically the stellar winds around massive stars, and explore the effect of rapid stellar rotation into radiation-driven winds. We present here the summary of the results obtained and conclusions of this work, and outline the ongoing and future projects related to the current topic of ffast-rotatinghot star winds.

After an overview of the literature of the previous works in the wind of massive stars Chap 1, we presented a general picture of radiation-driven winds and discussed the CAK line force based on Sobolev approximation in Chap 2. In Chap 3 we showed the influence of rapid stellar rotation based on the Roche model, and the presence of von Zeipel gravity darkening which governs the latitudinal variation of the mass flux of a rotating star. This results increase of the polar mass loss, opposite to the expected increase at the equator due to the centrifugal gravity weakening. Rapid rotation can lead to axisymmetric stellar wind, and due to electron scattering in such media, we can expect a nonzero polarization. The theory of radiation transfer is showed in Chap 4, where we discussed the mathematical formulation of the radiative transfer equation, and the Stokes vector of the polarization.

To solve the hydrodynamic set of equations and equation of radiative transfer, we discussed in Chap 5 the numerical methods used in astrophysics, we focused on the finite volume method, and the Monte Carlo method. The results of the hydrodynamic simulation are shown in Chap 6, and in Chap 7 we discussed the polarization from a point source, using single-scattering and multiple-scattering models.

We have revisited the line-driven wind models for various types of massive stars, ranging from optically thin winds to optically thick winds. To validate our model, we compared it with previous studies and found agreement with the semi-analytical model of BC and the numerical model of Owocki, Cranmer, and Blondin (1994), which only considered the radial force.

We went beyond these previous models and incorporated non-radial components and gravity darkening into our simulations. Interestingly, our results were similar to the findings of Owocki, Cranmer, and Gayley (1996) for Be and WR stars. The inclusion of non-radial forces inhibited disk formation and led to a reduction in density at the equator.

However, when studying low metallicity stars, we observed that some exhibited equatorial compression at high rotation rates (greater than 80% of the critical velocity). This suggests that the dynamics of line-driven winds in low metallicity stars are more complex and warrant further investigation.

We also computed the linear polarization resulting from electron scattering in the wind of Wolf Rayet stars through the ingenious formalism of Brown and McLean (1977), uncovering their potential as progenitors of long gamma-ray bursts. In addition, we embarked on a grand exploration to validate the analytical formulation, employing the power of Monte Carlo simulation to recreate polarization behavior in both optically thick and thin media. The findings were strikingly similar for modest rotations, while a discrepancy emerged when the rotations reached higher values. Intriguingly, the simulation revealed that multiple scatterings gave rise to unparalleled polarization, particularly at inclinations between 40 and 60 degrees. Furthermore, in optically thin media, both the analytical formulation and the Monte Carlo simulation dutifully presented a polarization directly proportional to the square of the sine of the inclination, echoing the seminal works of Brown and McLean.

8.2 Future work aspects

There is a lot of work that still needs to be done, both in advancing the theoretical work presented in this dissertation and in including novel physics in models of the winds of rotating massive stars. Although we explained the dynamics of Wolf Rayet stellar winds using the assumption that the wind is optically thin, similar to that of Be stars, in reality, these winds are thought to be optically thick. To address this in optically thick media, we started to use more advanced hydrodynamic codes that take radiation into account. We have recently started to incorporate fast rotation into the MPI-AMRVAC code, which includes a radiation module added by Moens et al. (2022).

Bibliography

Bianchi, Simone and Andrea Ferrara (Apr. 2005). “Intergalactic medium metal enrichment through dust sputtering”. In: *Monthly Notices of the RAS* 358.2, pp. 379–396. DOI: `10.1111/j.1365-2966.2005.08762.x`. arXiv: `astro-ph/0501147 [astro-ph]`.

Bjorkman, J. E. and J. P. Cassinelli (May 1993). “Equatorial Disk Formation around Rotating Stars Due to Ram Pressure Confinement by the Stellar Wind”. In: *The Astrophysical Journal* 409, p. 429. DOI: `10.1086/172676`.

Blondin, John M. et al. (June 1990). “Hydrodynamic Simulations of Stellar Wind Disruption by a Compact X-Ray Source”. In: *The Astrophysical Journal* 356, p. 591. DOI: `10.1086/168865`.

Bohren, Craig F. and Donald R. Huffman (1998). *Absorption and Scattering of Light by Small Particles*.

Brown, J. C., R. Ignace, and J. P. Cassinelli (Apr. 2000). “Hot star polarimetric variability and the nature of wind inhomogeneities”. In: *Astronomy & Astrophysics* 356, pp. 619–626.

Brown, J. C. and I. S. McLean (May 1977). “Polarisation by Thomson Scattering in Optically Thin Stellar Envelopes. I. Source Star at Centre of Axisymmetric Envelope”. In: *Astronomy & Astrophysics* 57, p. 141.

Cassinelli, J. P., K. H. Nordsieck, and M. A. Murison (June 1987). “Polarization of Light Scattered from the Winds of Early-Type Stars”. In: *The Astrophysical Journal* 317, p. 290. DOI: `10.1086/165277`.

Castor, J. I., D. C. Abbott, and R. I. Klein (Jan. 1975). “Radiation-driven winds in Of stars.” In: *The Astrophysical Journal* 195, pp. 157–174. DOI: `10.1086/153315`.

Castor, John I. (2007). *Radiation Hydrodynamics*.

Chandrasekhar, Subrahmanyan (1960). *Radiative transfer*.

Chang, Zhe, Yunguo Jiang, and Hai-Nan Lin (Dec. 2013). “Polarization of Photons Scattered By Electrons in any Spectral Distribution”. In: *The Astrophysical Journal* 780.1, p. 68. DOI: `10.1088/0004-637X/780/1/68`. URL: `https://dx.doi.org/10.1088/0004-637X/780/1/68`.

Che, X. et al. (May 2011). “Colder and Hotter: Interferometric Imaging of β Cassiopeiae and α Leonis”. In: *The Astrophysical Journal* 732.2, 68, p. 68. DOI: `10.1088/0004-637X/732/2/68`. arXiv: `1105.0740 [astro-ph.SR]`.

Chiosi, C., E. Nasi, and G. Bertelli (Apr. 1979). “Massive stars: evolution with mass-loss. II. Mass-loss in early phases, and evolutionary status of the transition Wolf Rayet stars.” In: *Astronomy & Astrophysics* 74, pp. 62–72.

Code, Arthur D. and Barbara A. Whitney (Mar. 1995). “Polarization from Scattering in Blobs”. In: *The Astrophysical Journal* 441, p. 400. DOI: `10.1086/175363`.

Colella, P. and Paul R. Woodward (Sept. 1984). “The Piecewise Parabolic Method (PPM) for Gas-Dynamical Simulations”. In: *Journal of Computational Physics* 54, pp. 174–201. DOI: 10.1016/0021-9991(84)90143-8.

Collins George W., II (Nov. 1963). “Continuum Emission from a Rapidly Rotating Stellar Atmosphere.” In: *The Astrophysical Journal* 138, p. 1134. DOI: 10.1086/147712.

— (1989). *The fundamentals of stellar astrophysics*.

Conti, P. S. (Jan. 1975). “On the relationship between Of and WR stars.” In: *Memoires of the Societe Royale des Sciences de Liege* 9, pp. 193–212.

Cotton, Daniel V. et al. (Sept. 2017). “Polarization due to rotational distortion in the bright star Regulus”. In: *Nature Astronomy* 1, pp. 690–696. DOI: 10.1038/s41550-017-0238-6. arXiv: 1804.06576 [astro-ph.SR].

Cranmer, Steven R. (Aug. 1996). “Dynamical Models of Winds from Rotating Hot Stars”. PhD thesis. Bartol Research Institute, University of Delaware.

Cranmer, Steven R. and Stanley P. Owocki (Feb. 1995). “The Effect of Oblateness and Gravity Darkening on the Radiation Driving in Winds from Rapidly Rotating B Stars”. In: *The Astrophysical Journal* 440, p. 308. DOI: 10.1086/175272.

Crowther, Paul A. (Sept. 2007). “Physical Properties of Wolf-Rayet Stars”. In: *Annual Review of Astronomy & Astrophysics* 45.1, pp. 177–219. DOI: 10.1146/annurev.astro.45.051806.110615. arXiv: astro-ph/0610356 [astro-ph].

Curé, M., D. F. Rial, and L. Cidale (July 2005). “Outflowing disk formation in B[e] supergiants due to rotation and bi-stability in radiation driven winds”. In: *Astronomy & Astrophysics* 437.3, pp. 929–933. DOI: 10.1051/0004-6361:20052686. arXiv: astro-ph/0503359 [astro-ph].

Curé, Michel (Oct. 2004). “The Influence of Rotation in Radiation-driven Wind from Hot Stars: New Solutions and Disk Formation in Be Stars”. In: *The Astrophysical Journal* 614.2, pp. 929–941. DOI: 10.1086/423776. arXiv: astro-ph/0406490 [astro-ph].

Domiciano de Souza, A. et al. (Sept. 2014). “The environment of the fast rotating star Achernar. III. Photospheric parameters revealed by the VLTI”. In: *Astronomy & Astrophysics* 569, A10, A10. DOI: 10.1051/0004-6361/201424144.

Donati, J. F. et al. (Jan. 2002). “High-Resolution Spectropolarimetry on the VLT”. In: *Scientific Drivers for ESO Future VLT/VLTI Instrumentation*. Ed. by Jaqueline Bergeron and Guy Monnet, p. 238. DOI: 10.1007/10857019_37.

Dwarkadas, Vikram V. and Stanley P. Owocki (Dec. 2002). “Radiatively Driven Winds and the Shaping of Bipolar Luminous Blue Variable Nebulae”. In: *The Astrophysical Journal* 581.2, pp. 1337–1343. DOI: 10.1086/344257.

Espinosa Lara, F. and M. Rieutord (Sept. 2011). “Gravity darkening in rotating stars”. In: *Astronomy & Astrophysics* 533, A43, A43. DOI: 10.1051/0004-6361/201117252. arXiv: 1109.3038 [astro-ph.SR].

— (Nov. 2012). “Gravity darkening in binary stars”. In: *Astronomy & Astrophysics* 547, A32, A32. DOI: 10.1051/0004-6361/201219942. arXiv: 1210.4004 [astro-ph.SR].

Evans, C. J. et al. (June 2011). “The VLT-FLAMES Tarantula Survey. I. Introduction and observational overview”. In: *Astronomy & Astrophysics* 530, A108, A108. DOI: 10.1051/0004-6361/201116782. arXiv: 1103.5386 [astro-ph.SR].

Feldmeier, A. et al. (Apr. 1997). “The X-ray emission from shock cooling zones in O star winds.” In: *Astronomy & Astrophysics* 320, pp. 899–912.

Fox, G. K. (Oct. 1993). “The Theoretical Polarization from Axisymmetric Circumstellar Envelopes with Constant Scattering Optical Depth”. In: *Monthly Notices of the RAS* 264, p. 565. DOI: `10.1093/mnras/264.3.565`.

Friend, D. B. and J. P. Cassinelli (Apr. 1986). “Polarization in Massive X-Ray Binaries. I. A Low-Inclination Model for Cygnus X-1”. In: *The Astrophysical Journal* 303, p. 292. DOI: `10.1086/164074`.

Friend, David B. and David C. Abbott (Dec. 1986). “The Theory of Radiatively Driven Stellar Winds. III. Wind Models with Finite Disk Correction and Rotation”. In: *The Astrophysical Journal* 311, p. 701. DOI: `10.1086/164809`.

Fryxell, B. et al. (Nov. 2000). “FLASH: An Adaptive Mesh Hydrodynamics Code for Modeling Astrophysical Thermonuclear Flashes”. In: *The Astrophysical Journal Supplement Series* 131.1, p. 273. DOI: `10.1086/317361`. URL: `https://dx.doi.org/10.1086/317361`.

Gayley, Kenneth G. (Nov. 1995). “An Improved Line-Strength Parameterization in Hot-Star Winds”. In: *The Astrophysical Journal* 454, p. 410. DOI: `10.1086/176492`.

Gräfener, G. et al. (Nov. 2012). “Rotating Wolf-Rayet stars in a post RSG/LBV phase. An evolutionary channel towards long-duration GRBs?” In: *Astronomy & Astrophysics* 547, A83, A83. DOI: `10.1051/0004-6361/201118664`. arXiv: `1210.1153 [astro-ph.SR]`.

Grunhut, J. H. et al. (Feb. 2017). “The MiMeS survey of Magnetism in Massive Stars: magnetic analysis of the O-type stars”. In: *Monthly Notices of the RAS* 465.2, pp. 2432–2470. DOI: `10.1093/mnras/stw2743`. arXiv: `1610.07895 [astro-ph.SR]`.

Halonen, Robbie J. and Carol E. Jones (Sept. 2013). “On the Intrinsic Continuum Linear Polarization of Classical Be Stars: The Effects of Metallicity and One-armed Density Perturbations”. In: *The Astrophysical Journal Supplement* 208.1, 3, p. 3. DOI: `10.1088/0067-0049/208/1/3`. arXiv: `1307.6220 [astro-ph.SR]`.

Harries, Tim J. (July 2000). “Synthetic line profiles of rotationally distorted hot-star winds”. In: *Monthly Notices of the RAS* 315.4, pp. 722–734. DOI: `10.1046/j.1365-8711.2000.03505.x`.

Hillier, D. John and D. L. Miller (Mar. 1998). “The Treatment of Non-LTE Line Blanketing in Spherically Expanding Outflows”. In: *The Astrophysical Journal* 496.1, pp. 407–427. DOI: `10.1086/305350`.

Huang, Wenjin, D. R. Gies, and M. V. McSwain (Oct. 2010). “A Stellar Rotation Census of B Stars: From ZAMS to TAMS”. In: *The Astrophysical Journal* 722.1, pp. 605–619. DOI: `10.1088/0004-637X/722/1/605`. arXiv: `1008.1761 [astro-ph.SR]`.

Hubeny, Ivan and Dimitri Mihalas (2015). *Theory of Stellar Atmospheres. An Introduction to Astrophysical Non-equilibrium Quantitative Spectroscopic Analysis*.

Ignace, R., J. P. Cassinelli, and J. E. Bjorkman (Mar. 1996). “Equatorial Wind Compression Effects across the H-R Diagram”. In: *The Astrophysical Journal* 459, p. 671. DOI: `10.1086/176932`.

Krtička, J. and A. Feldmeier (Sept. 2018). “Light variations due to the line-driven wind instability and wind blanketing in O stars”. In: *Astronomy & Astrophysics* 617, A121, A121. DOI: `10.1051/0004-6361/201731614`. arXiv: `1807.09407 [astro-ph.SR]`.

Krtička, J. and J. Kubát (Oct. 2017). "Comoving frame models of hot star winds. II. Reduction of O star wind mass-loss rates in global models". In: *Astronomy & Astrophysics* 606, A31, A31. doi: `10.1051/0004-6361/201730723`. arXiv: `1706.06194 [astro-ph.SR]`.

Kubátová, B. et al. (Mar. 2019). "Low-metallicity massive single stars with rotation. II. Predicting spectra and spectral classes of chemically homogeneously evolving stars". In: *Astronomy & Astrophysics* 623, A8, A8. doi: `10.1051/0004-6361/201834360`. arXiv: `1810.01267 [astro-ph.SR]`.

Lamers, Henny J. G. L. M. and Joseph P. Cassinelli (1999). *Introduction to Stellar Winds*.

Lax, Peter and Burton Wendroff (1960). "Systems of conservation laws". In: *Communications on Pure and Applied Mathematics* 13.2, pp. 217–237. doi: `https://doi.org/10.1002/cpa.3160130205`. eprint: `https://onlinelibrary.wiley.com/doi/pdf/10.1002/cpa.3160130205`. url: `https://onlinelibrary.wiley.com/doi/abs/10.1002/cpa.3160130205`.

LeVeque, Randall J et al. (2002). *Finite volume methods for hyperbolic problems*. Vol. 31. Cambridge university press.

Lee, Umin, Yoji Osaki, and Hideyuki Saio (May 1991). "Viscous excretion discs around Be stars". In: *Monthly Notices of the RAS* 250, pp. 432–437. doi: `10.1093/mnras/250.2.432`.

Lucy, L. B. and P. M. Solomon (Mar. 1970). "Mass Loss by Hot Stars". In: *The Astrophysical Journal* 159, p. 879. doi: `10.1086/150365`.

MacFadyen, A. I. and S. E. Woosley (Oct. 1999). "Collapsars: Gamma-Ray Bursts and Explosions in "Failed Supernovae"". In: *The Astrophysical Journal* 524.1, pp. 262–289. doi: `10.1086/307790`. arXiv: `astro-ph/9810274 [astro-ph]`.

Maeder, André (2009). *Physics, Formation and Evolution of Rotating Stars*. doi: `10.1007/978-3-540-76949-1`.

McLean, I. S. (Jan. 1979). "Interpretation of the intrinsic polarization of early-type emission-line stars." In: *Monthly Notices of the RAS* 186, pp. 265–285. doi: `10.1093/mnras/186.2.265`.

Mignone, A. et al. (May 2007). "PLUTO: A Numerical Code for Computational Astrophysics". In: *The Astrophysical Journal Supplement* 170.1, pp. 228–242. doi: `10.1086/513316`. arXiv: `astro-ph/0701854 [astro-ph]`.

Moens, N. et al. (Sept. 2022). "First 3D radiation-hydrodynamic simulations of Wolf-Rayet winds". In: *Astronomy & Astrophysics* 665, A42, A42. doi: `10.1051/0004-6361/202243451`. arXiv: `2203.01108 [astro-ph.SR]`.

Neumann, J. von (1951). *Applied Math Series*. Vol. 12. 1.

Noebauer, Ulrich M. and Stuart A. Sim (June 2019). "Monte Carlo radiative transfer". In: *Living Reviews in Computational Astrophysics* 5.1, 1, p. 1. doi: `10.1007/s41115-019-0004-9`. arXiv: `1907.09840 [astro-ph.IM]`.

Owocki, S. P., S. R. Cranmer, and K. G. Gayley (Dec. 1996). "Inhibition FO Wind Compressed Disk Formation by Nonradial Line-Forces in Rotating Hot-Star Winds". In: *The Astrophysical Journal Letters* 472, p. L115. doi: `10.1086/310372`.

Owocki, S. P. and J. Puls (Jan. 1999). "Line-driven Stellar Winds: The Dynamical Role of Diffuse Radiation Gradients and Limitations to the Sobolev Approach". In: *The Astrophysical Journal* 510.1, pp. 355–368. doi: `10.1086/306561`.

Owocki, S. (Dec. 2012). “The Dynamical Role of Radiative Driving in the Sources and Sinks of Circumstellar Matter in Massive Stars”. In: *Circumstellar Dynamics at High Resolution*. Ed. by A. C. Carciofi and Th. Rivinius. Vol. 464. Astronomical Society of the Pacific Conference Series, p. 255.

Owocki, Stan (2013). “Stellar Winds”. In: *Planets, Stars and Stellar Systems: Volume 4: Stellar Structure and Evolution*. Ed. by Terry D. Oswalt and Martin A. Barstow. Dordrecht: Springer Netherlands, pp. 735–788. ISBN: 978-94-007-5615-1. DOI: `10.1007/978-94-007-5615-1_15`. URL: `https://doi.org/10.1007/978-94-007-5615-1_15`.

Owocki, Stanley P., John I. Castor, and George B. Rybicki (Dec. 1988). “Time-dependent Models of Radiatively Driven Stellar Winds. I. Nonlinear Evolution of Instabilities for a Pure Absorption Model”. In: *The Astrophysical Journal* 335, p. 914. DOI: `10.1086/166977`.

Owocki, Stanley P., Steven R. Cranmer, and John M. Blondin (Apr. 1994). “Two-dimensional Hydrodynamical Simulations of Wind-compressed Disks around Rapidly Rotating B Stars”. In: *The Astrophysical Journal* 424, p. 887. DOI: `10.1086/173938`.

Parker, E. N. (Nov. 1960). “The Hydrodynamic Theory of Solar Corpuscular Radiation and Stellar Winds.” In: *The Astrophysical Journal* 132, p. 821. DOI: `10.1086/146985`.

Pauldrach, A., J. Puls, and R. P. Kudritzki (Aug. 1986). “Radiation-driven winds of hot luminous stars. Improvements of the theory and first results.” In: *Astronomy & Astrophysics* 164, pp. 86–100.

Puls, J., U. Springmann, and M. Lennon (Jan. 2000). “Radiation driven winds of hot luminous stars. XIV. Line statistics and radiative driving”. In: *Astronomy & Astrophysics Supplement Series* 141, pp. 23–64. DOI: `10.1051/aas:2000312`.

Puls, J. et al. (Aug. 2006). “Bright OB stars in the Galaxy. III. Constraints on the radial stratification of the clumping factor in hot star winds from a combined H_α, IR and radio analysis”. In: *Astronomy & Astrophysics* 454.2, pp. 625–651. DOI: `10.1051/0004-6361:20065073`. arXiv: `astro-ph/0604372 [astro-ph]`.

Rieutord, M. and F. Espinosa Lara (July 2009). “On the dynamics of a radiative rapidly rotating star”. In: *Communications in Asteroseismology* 158, p. 99.

Robitaille, T. P. (Dec. 2011). “HYPERION: an open-source parallelized three dimensional dust continuum radiative transfer code”. In: *Astronomy & Astrophysics* 536, A79, A79. DOI: `10.1051/0004-6361/201117150`. arXiv: `1112.1071 [astro-ph.IM]`.

Sander, A., W. R. Hamann, and H. Todt (Apr. 2012). “The Galactic WC stars. Stellar parameters from spectral analyses indicate a new evolutionary sequence”. In: *Astronomy & Astrophysics* 540, A144, A144. DOI: `10.1051/0004-6361/201117830`. arXiv: `1201.6354 [astro-ph.SR]`.

Schulte-Ladbeck, Regina E. (Nov. 1994). “Spectropolarimetry of Hot, Luminous Stars”. In: *Astrophysics and Space Science* 221.1-2, pp. 347–356. DOI: `10.1007/BF01091165`.

Shepard, Katherine et al. (Jan. 2020). “HST/COS Spectra of the Wind Lines of VFTS 102 and 285”. In: *The Astrophysical Journal* 888.2, p. 82. DOI: `10.3847/1538-4357/ab5a82`. URL: `https://dx.doi.org/10.3847/1538-4357/ab5a82`.

Shepard, Katherine et al. (May 2022). "Spectroscopic Line Modeling of the Fastest Rotating O-type Stars". In: *The Astrophysical Journal* 931.1, 35, p. 35. DOI: `10.3847/1538-4357/ac66e6`. arXiv: `2204.07473 [astro-ph.SR]`.

Shrestha, Manisha et al. (June 2018). "Polarization simulations of stellar wind bow-shock nebulae - I. The case of electron scattering". In: *Monthly Notices of the RAS* 477.1, pp. 1365–1382. DOI: `10.1093/mnras/sty724`. arXiv: `1712.04958 [astro-ph.SR]`.

Springel, Volker (2016). "High Performance Computing and Numerical Modelling". In: *Star Formation in Galaxy Evolution: Connecting Numerical Models to Reality: Saas-Fee Advanced Course 43. Swiss Society for Astrophysics and Astronomy*. Ed. by Yves Revaz et al. Berlin, Heidelberg: Springer Berlin Heidelberg, pp. 251–358. ISBN: 978-3-662-47890-5. DOI: `10.1007/978-3-662-47890-5_3`. URL: `https://doi.org/10.1007/978-3-662-47890-5_3`.

Stevance, H. F. et al. (Oct. 2018). "Probing the rotational velocity of Galactic WO stars with spectropolarimetry". In: *Monthly Notices of the RAS* 479.4, pp. 4535–4543. DOI: `10.1093/mnras/sty1827`. arXiv: `1807.02117 [astro-ph.SR]`.

Stone, James M. et al. (June 2020). "The Athena++ Adaptive Mesh Refinement Framework: Design and Magnetohydrodynamic Solvers". In: *The Astrophysical Journal Supplement Series* 249.1, p. 4. DOI: `10.3847/1538-4365/ab929b`. URL: `https://doi.org/10.3847%2F1538-4365%2Fab929b`.

Sundqvist, J. O., J. Puls, and A. Feldmeier (Jan. 2010). "Mass loss from inhomogeneous hot star winds. I. Resonance line formation in 2D models". In: *Astronomy & Astrophysics* 510, A11, A11. DOI: `10.1051/0004-6361/200912842`. arXiv: `0911.3361 [astro-ph.SR]`.

Sundqvist, J. O. et al. (Dec. 2019). "New predictions for radiation-driven, steady-state mass-loss and wind-momentum from hot, massive stars. I. Method and first results". In: *Astronomy & Astrophysics* 632, A126, A126. DOI: `10.1051/0004-6361/201936580`. arXiv: `1910.06586 [astro-ph.SR]`.

Šurlan, B. et al. (May 2013). "Modelling of Resonance Lines in Inhomogeneous Hot Star Winds". In: *Publications de l'Observatoire Astronomique de Beograd* 92, pp. 197–200.

Townsend, R. H. D., S. P. Owocki, and I. D. Howarth (May 2004). "Be-star rotation: how close to critical?" In: *Monthly Notices of the RAS* 350.1, pp. 189–195. DOI: `10.1111/j.1365-2966.2004.07627.x`. arXiv: `astro-ph/0312113 [astro-ph]`.

Townsend, Rich (May 2012). "A Monte-Carlo method for simulating linear polarization variations in clumpy massive-star winds". In: *Stellar Polarimetry: from Birth to Death*. Ed. by Jennifer L. Hoffman, Jon Bjorkman, and Barbara Whitney. Vol. 1429. American Institute of Physics Conference Series, pp. 278–281. DOI: `10.1063/1.3701941`.

Tramper, F. et al. (Sept. 2015). "Massive stars on the verge of exploding: the properties of oxygen sequence Wolf-Rayet stars". In: *Astronomy & Astrophysics* 581, A110, A110. DOI: `10.1051/0004-6361/201425390`. arXiv: `1507.00839 [astro-ph.SR]`.

Vink, Jorick S. and A. de Koter (Nov. 2005). "On the metallicity dependence of Wolf-Rayet winds". In: *Astronomy & Astrophysics* 442.2, pp. 587–596. DOI: `10.1051/0004-6361:20052862`. arXiv: `astro-ph/0507352 [astro-ph]`.

Vink, Jorick S., A. de Koter, and H. J. G. L. M. Lamers (Apr. 2001). "Mass-loss predictions for O and B stars as a function of metallicity". In: *Astronomy & Astrophysics* 369, pp. 574–588. DOI: 10.1051/0004-6361:20010127. arXiv: astro-ph/0101509 [astro-ph].

Vink, Jorick S. et al. (Nov. 2002). “Probing the circumstellar structure of Herbig Ae/Be stars”. In: *Monthly Notices of the RAS* 337.1, pp. 356–368. DOI: 10.1046/j.1365-8711.2002.05920.x. arXiv: astro-ph/0208137 [astro-ph].

Vink, Jorick S. et al. (July 2011). “Wind modelling of very massive stars up to 300 solar masses”. In: *Astronomy & Astrophysics* 531, A132, A132. DOI: 10.1051/0004-6361/201116614. arXiv: 1105.0556 [astro-ph.SR].

Whitney, B. A. (Mar. 2011). “Monte Carlo radiative transfer”. In: *Bulletin of the Astronomical Society of India* 39, pp. 101–127. DOI: 10.1016/j.icarus.2012.11.018. arXiv: 1104.4990 [astro-ph.SR].

Wood, Kenneth et al. (Apr. 1996). “The Effect of Multiple Scattering on the Polarization from Axisymmetric Circumstellar Envelopes. I. Pure Thomson Scattering Envelopes”. In: *The Astrophysical Journal* 461, p. 828. DOI: 10.1086/177105.

Woosley, S. E. (Mar. 1993). “Gamma-Ray Bursts from Stellar Mass Accretion Disks around Black Holes”. In: *The Astrophysical Journal* 405, p. 273. DOI: 10.1086/172359.

Woosley, S. E., Ronald G. Eastman, and Brian P. Schmidt (May 1999). “Gamma-Ray Bursts and Type IC Supernova SN 1998BW”. In: *The Astrophysical Journal* 516.2, pp. 788–796. DOI: 10.1086/307131. arXiv: astro-ph/9806299 [astro-ph].

ud-Doula, Asif (2002). “"The Effects of Magnetic Fields and Field-Aligned Rotation on Line-Drived Hot-Star Winds"”. PhD thesis.

van Belle, Gerard T. et al. (Oct. 2001). “Altair’s Oblateness and Rotation Velocity from Long-Baseline Interferometry”. In: *The Astrophysical Journal* 559.2, pp. 1155–1164. DOI: 10.1086/322340.

von Zeipel, H. (June 1924). “The radiative equilibrium of a rotating system of gaseous masses”. In: *Monthly Notices of the RAS* 84, pp. 665–683. DOI: 10.1093/mnras/84.9.665.